

# A New Variational Model for Joint Image Reconstruction and Motion Estimation in Spatiotemporal Imaging

Chong Chen<sup>\*</sup>, Barbara Gris<sup>†</sup> and Ozan Öktem<sup>‡</sup>

## Abstract

We propose a new variational model for joint image reconstruction and motion estimation in spatiotemporal imaging, which is investigated along a general framework that we present with shape theory. This model consists of two components, one for conducting modified static image reconstruction, and the other performs sequentially indirect image registration. For the latter, we generalize the large deformation diffeomorphic metric mapping framework into the sequentially indirect registration setting. The proposed model is compared theoretically against alternative approaches (optical flow based model and diffeomorphic motion models), and we demonstrate that the proposed model has desirable properties in terms of the optimal solution. The theoretical derivations and efficient algorithms are also presented for a time-discretized scenario of the proposed model, which show that the optimal solution of the time-discretized version is consistent with that of the time-continuous one, and most of the computational components is the easy-implemented linearized deformation. The complexity of the algorithm is analyzed as well. This work is concluded by some numerical examples in 2D space + time tomography with very sparse and/or highly noisy data.

**Keywords:** spatiotemporal imaging, image reconstruction, motion estimation, joint variational model, shape theory, large diffeomorphic deformations

## 1 Introduction

Image reconstruction is challenging in a spatiotemporal setting when the object being imaged undergoes a temporal evolution. This is the case in tomographic imaging of the heart or lung [13, 28] where it is important to estimate and compensate for the unknown motion of the organs. As an example, data in positron emission tomography (PET) cardiac imaging is acquired over a relatively long period of time (often in the range of minutes). The respiratory and cardiac motion cause a displacement of 20-40 mm to organs of interest [47, 58]. Failing to correct for such motion leads to a degradation in image quality [28].

<sup>\*</sup>LSEC, ICMSEC, Academy of Mathematics and Systems Science, Chinese Academy of Sciences, Beijing 100190, China (chench@lsec.cc.ac.cn).

<sup>†</sup>LJLL–Laboratoire Jacques-Louis Lions, Sorbonne Université, 75005 Paris, France (bgris.maths@gmail.com).

<sup>‡</sup>Department of Mathematics, KTH–Royal Institute of Technology, 10044 Stockholm, Sweden (ozan@kth.se).

Data in spatiotemporal imaging is a time or quasi-time series and one obvious approach is to decompose it into sub-sets (gates) such that data within each gate is generated by the object in a fixed temporal state [24, 34, 36]. Much work has been done along these lines in the context of PET imaging of the heart or lung, where each gate is the phase of breathing and/or cardiac motion [22, 31, 15]. One also studies on how to optimize the gating in order to obtain the optimal image quality by reconstruction [26, 56].

Once data is gated, algorithms for spatiotemporal image reconstruction can be separated into two categories: first image reconstruction then motion estimation; joint image reconstruction and motion estimation [7, 28]. In the first category, one starts with applying static image reconstruction on data from each of the gates, resulting in a series of (low-resolution) images, then selects a reconstructed image as target and registers the other reconstructed images against this target, finally averages all the registered images to obtain the reconstructed image (see, for example, [2, 3, 21, 23, 29, 28]). The second category is establishing the joint tasks of image reconstruction and motion estimation into one model, then gaining the optimal solution to reconstruct the image in each gate. This is more complex and several approaches have been suggested for how to do this, such as [7, 46, 50, 27, 35, 9, 8, 43, 33, 51, 6, 32, 32, 10, 13], and so forth.

The approach taken in this paper belongs to the second category and the motion model makes use of diffeomorphic deformations. The latter are provided by the large deformation diffeomorphic metric mapping (LDDMM) framework, which is a well-developed framework for diffeomorphic image registration (see, for instance, [53, 25, 37, 5, 30, 60, 54, 55, 11, 12]). Diffeomorphic deformations based on LDDMM were used in [32] for joint image reconstruction and motion estimation in 4D computed tomography (CT), which is based on the growth model of LDDMM [30]. Later they were also used in [17] for indirect image registration. Nevertheless, this paper is dedicated to proposing a new joint variational model based on the principle of LDDMM.

**Contributions** The main contribution is a new variational model for joint image reconstruction and motion estimation in spatiotemporal imaging based on the LDDMM framework, which is studied along a general framework of variational model that we present with deformable templates from shape theory. This model contains two components: one corresponding to modified static image reconstruction, and the other corresponding to sequentially indirect image registration. For the latter, we generalize the LDDMM framework into the sequentially indirect registration setting.

The mathematical properties of the proposed variational model is compared against the optical flow based model in [13] and the diffeomorphic motion model in [32]. The comparison shows that the proposed model has some desirable properties in terms of the optimal solution, for example, guaranteeing elastically large diffeomorphic deformations, averagely distributed w.r.t. time  $t$ , and non-vanishing neither on the initial nor on the end time point, etc. Moreover, a computationally efficient gradient-based iterative scheme is presented for the time-discretized version. More importantly, the optimal solution of the time-discretized problem is consistent with that of the time-continuous one. Most of the computationally demanding parts relate to implementing the linearized deformations [42].

**Outline** A general variational model for joint image reconstruction and motion estimation is presented in section 2. For self-contained, we revisit LDDMM briefly in section 3.1, then propose the new variational model in section 3.2. The section 3.3 makes the mathematical comparison between the proposed model and the existing models. The section 4 gives the detailed numerical algorithms for solving the proposed model. The numerical experiments are performed in section 5 to show the performance of the new model with 2D + time tomography. Finally, the section 6 concludes the paper.

## 2 A general variational model for joint image reconstruction and motion estimation

The spatiotemporal (space + time) image reconstruction is typically a spatiotemporal inverse problem. The aim is to estimate a spatially distributed quantity (image) that exhibits temporal variations from indirect time-dependent noisy observations (measured data). Hence, both the image and its motion are unknown.

### 2.1 General spatiotemporal inverse problem

Let  $f: [t_0, t_1] \times \Omega \rightarrow \mathbb{R}^k$  denote the spatiotemporal image that we need to reconstruct. Here  $k$  is the number of modalities (often  $k = 1$ ) and  $\Omega \subset \mathbb{R}^n$  is spatial domain. Without loss of generality, the general (quasi-)time domain  $[t_0, t_1]$  can be reparameterized onto  $[0, 1]$ .

The spatiotemporal inverse problem is to reconstruct a spatiotemporal image  $f(t, \cdot) \in \mathcal{X}$  from measured data  $g(t, \cdot) \in \mathcal{Y}$  such that

$$g(t, \cdot) = \mathcal{T}(t, f(t, \cdot)) + g_{\text{noise}}(t, \cdot) \quad \text{for } t \in [0, 1], \quad (1)$$

where  $\mathcal{X}$  (reconstruction space) is the vector space of all possible images on a fixed domain  $\Omega$ ,  $\mathcal{Y}$  (data space) is the vector space of all possible data, and  $g_{\text{noise}}(t, \cdot) \in \mathcal{Y}$  is the observation noise in data. Furthermore,  $\mathcal{T}(t, \cdot): \mathcal{X} \rightarrow \mathcal{Y}$  is a time-dependent forward operator, for short denoted by  $\mathcal{T}_t$ , that models how an image at time  $t$  gives rise to data in absence of noise or measurement errors (e.g., a stack of Radon transforms with various geometric parameters of scanning for CT and PET and attenuated Radon transform instead for single photon emission computed tomography (SPECT), etc.) [40]. Note that for spatiotemporal problems, the collection of geometric parameters of scanning is basically different in the temporal direction.

A key step is to further specify the form of the spatiotemporal image  $f(t, \cdot)$  and here we will use the idea of deformable templates from shape theory.

### 2.2 Spatiotemporal inverse problem based on shape theory

Shape theory seeks to develop quantitative tools to study shapes and their variability, which can be pursued to work of D’Arcy Thompson [52]. Shapes of objects are considered as points in the shape space [55]. The collections of deformable objects and deformations need to be defined. The former represent the objects whose shape we want to analyze, the latter are transformations that can act on the deformable objects. The underlying idea is that shapes

are represented as a deformation of a template, so the template represents the “shape invariant” part of the object whereas the set of deformations model how various shapes arise. Shape similarity between two objects can then be quantified as the “cost” of deforming one object into the other by means of a minimal deformation in the set of deformations. For more details, the reader is referred to [60, 30, 39].

Based on the thought above, the spatial and temporal components of a spatiotemporal image can be separated as

$$f(t, \cdot) := \mathcal{W}(\phi_t, I) \quad \text{for some } \phi_t \in \mathcal{G} \text{ and } I \in \mathcal{X}. \quad (2)$$

Here  $\mathcal{W}: \mathcal{G} \times \mathcal{X} \rightarrow \mathcal{X}$  is a temporal evolution operator and  $\mathcal{G}$  is the group of diffeomorphisms on  $\Omega$ , i.e., the set of invertible mappings that are continuously differentiable with a continuously differentiable inverse from  $\Omega$  to  $\Omega$ . It is natural to require that  $\mathcal{W}$  is a group action of  $\mathcal{G}$  on  $\mathcal{X}$ , so we can write  $\mathcal{W}(\phi_t, I) := \phi_t \cdot I$  for simplicity. Furthermore,  $I: \Omega \rightarrow \mathbb{R}$  (template) is the time-independent spatial component and the deformation  $\phi_t: \Omega \rightarrow \Omega$  governs the temporal evolution of the template.

Therefore, the inverse problem in spatiotemporal imaging can now be written as

$$g(t, \cdot) = \mathcal{T}_t(\phi_t \cdot I) + g_{\text{noise}}(t, \cdot) \quad \text{for } t \in [0, 1]. \quad (3)$$

Notice that  $f(t, \cdot) = \phi_t \cdot I$  is the spatiotemporal image at time  $t$  generated from the template  $I$  and the deformation  $\phi_t$ . Hence, the above inverse problem calls for simultaneously recovering the time-independent template  $I$  and the time-dependent deformation  $\phi_t$ .

**Common group actions** A natural group action is the one that gives geometric deformations [17]:

$$\phi_t \cdot I = I \circ \phi_t^{-1}, \quad (4)$$

where “ $\circ$ ” denotes function composition. This group action yields a deformation that merely moves the position of the pixel/voxel but does not change its intensity.

An alternative group action is the one that corresponds to mass-preserving deformations [17, 60]:

$$\phi_t \cdot I = |D(\phi_t^{-1})| I \circ \phi_t^{-1}, \quad (5)$$

where  $|D(\phi)|$  denotes the determinant of the Jacobian of  $\phi$ . This group action adjusts the intensity values but preserves the total mass.

### 2.3 A general framework of joint image reconstruction and motion estimation

First of all, through simple analysis, it is not difficult to observe that the whole inverse problem (3) can be divided into two small subproblems. With given evolution deformation  $\phi_t$ , the original problem boils down to a modified static image reconstruction problem: one just needs to reconstruct template “ $I$ ” from noisy measured data. Since the data sets are measured from deformed template by known deformations, we name it with “modified”. On the other hand, with given template  $I$ , the remaining goal is to estimate the evolution parameter “ $\phi_t$ ”

from noisy measured data. We call it sequentially indirect image registration, which is a generalization of indirect image registration [17].

The inverse problem in (3) is ill-posed due to a variety of reasons. A variational formulation offers a flexible framework for regularizing a wide range of inverse problems [45]. The idea is to add regularization functionals penalize a maximum likelihood solution and thereby act as stabilisers.

In (3) we seek to recover both the template  $I \in \mathcal{X}$  and the temporal deformation  $\phi_t \in \mathcal{G}$  simultaneously from time-series data  $g(t, \cdot) \in \mathcal{Y}$ . A general variational model for this inverse problem reads as

$$\min_{\substack{I \in \mathcal{X} \\ \phi_t \in \mathcal{G}}} \left\{ \int_0^1 \left[ \mathcal{D}(\mathcal{T}_t(\phi_t \cdot I), g(t, \cdot)) dt + \mu_2 \mathcal{R}_2(\phi_t) \right] dt + \mu_1 \mathcal{R}_1(I) \right\}, \quad (6)$$

where  $\mu_1, \mu_2$  are nonnegative regularization parameters.

The above  $\mathcal{D} : \mathcal{Y} \times \mathcal{Y} \rightarrow \mathbb{R}_+$  is the data discrepancy functional quantifying the mismatch in data space  $\mathcal{Y}$  that is often designed as the form of  $\mathcal{L}^p$ -norm or Kullback-Leibler (KL) divergence. The above  $\mathbb{R}_+$  denotes the set of nonnegative real number. The selection of  $\mathcal{D}$  depends generally on the distribution of the noise in data, e.g., applying squared  $\mathcal{L}^2$ -norm

$$\mathcal{D}(g_1, g_2) := \|g_1 - g_2\|_2^2 \quad (7)$$

to Gaussian distribution and KL divergence

$$\mathcal{D}(g_1, g_2) := \int_{\Omega_{\mathcal{Y}}} g_1(y) - g_2(y) \ln(g_1(y)) dy \quad (8)$$

to Poisson distribution and for  $g_1, g_2 \in \mathcal{Y}$ .

Moreover, the spatial regularization  $\mathcal{R}_1 : \mathcal{X} \rightarrow \mathbb{R}_+$  introduces well-posedness by encoding priori knowledge about the image  $f$ , which is frequently based on the form of  $\mathcal{L}^p$ -norm of its gradient magnitude or certain sparse representation. Typically, taking the squared  $\mathcal{L}^2$ -norm of the gradient magnitude

$$\mathcal{R}_1(f) := \|\nabla f\|_2^2 \quad (9)$$

is known to produce smooth images whereas selecting the  $\mathcal{L}^1$ -norm of the gradient magnitude, i.e., total variation (TV) regularization

$$\mathcal{R}_1(f) := \|\nabla f\|_1 \quad (10)$$

yields edge-preserving images [44].

Subsequently, the key problem is to describe how to generate the evolution deformation  $\phi_t$  and to select shape regularization  $\mathcal{R}_2 : \mathcal{G} \rightarrow \mathbb{R}_+$  for the  $\phi_t$ . We will consider this problem within the LDDMM framework.

### 3 A new variational model for joint image reconstruction and motion estimation

This section introduces a new variational model of the framework (6) based on LDDMM. First we recall the basic principle of LDDMM for self-contained, and then give the proposed model.

### 3.1 The LDDMM framework

The LDDMM framework outlined here offers a generic way to generate a flow of diffeomorphisms through velocity field. In this framework, the linearized deformation is considered as infinitesimal deformation, and the displacement field is seen as an instantaneous velocity field. Under certain regularity, the composition of such small deformations in the limit generates a flow of diffeomorphisms given as the solution to an ordinary differential equation (ODE) [60].

More precisely, given a velocity field  $\boldsymbol{\nu} : [0, 1] \times \Omega \rightarrow \mathbb{R}^n$ , a flow  $\phi_t$  is generated by the following ODE:

$$\begin{cases} \partial_t \phi_t(x) = \boldsymbol{\nu}(t, \phi_t(x)) \\ \phi_0(x) = x \end{cases} \quad \text{for } x \in \Omega \text{ and } 0 \leq t \leq 1. \quad (11)$$

Note that  $\phi_0 = \text{Id}$ , i.e., the flow starts at the identity deformation (mapping). If the velocity field  $\boldsymbol{\nu}$  is sufficiently regular, then the solution to the above ODE is well-defined and that becomes a flow of diffeomorphisms. We subsequently define the precise notion of regularity that is needed.

**Definition 1** (Admissible space [60]). A Hilbert space  $\mathcal{V} \subset \mathcal{C}_0^1(\Omega, \mathbb{R}^n)$  is admissible if it is (canonically) embedded in  $\mathcal{C}_0^1(\Omega, \mathbb{R}^n)$  with the  $\|\cdot\|_{1,\infty}$  norm, i.e., there exists a constant  $C > 0$  such that

$$\|\nu\|_{1,\infty} \leq C \|\nu\|_{\mathcal{V}} \quad \text{for all } \nu \in \mathcal{V}.$$

In the above,  $\|\nu\|_{1,\infty} := \|\nu\|_1 + \|D\nu\|_{\infty}$  for  $\nu \in \mathcal{C}_0^1(\Omega, \mathbb{R}^n)$ .

Then a proper space of velocity fields is well-defined as

$$\mathcal{L}^p([0, 1], \mathcal{V}) := \left\{ \boldsymbol{\nu} : \boldsymbol{\nu}(t, \cdot) \in \mathcal{V} \text{ and } \|\boldsymbol{\nu}\|_{\mathcal{L}^p([0,1], \mathcal{V})} < \infty \text{ for } 1 \leq p \leq \infty \right\} \quad (12)$$

with the associated norm

$$\|\boldsymbol{\nu}\|_{\mathcal{L}^p([0,1], \mathcal{V})} := \left( \int_0^1 \|\boldsymbol{\nu}(t, \cdot)\|_{\mathcal{V}}^p dt \right)^{1/p}.$$

For short, let  $\mathcal{L}_{\mathcal{V}}^p(\Omega)$  denote  $\mathcal{L}^p([0, 1], \mathcal{V})$ . Note that  $\mathcal{L}_{\mathcal{V}}^2(\Omega)$  is a Hilbert space with inner product

$$\langle \boldsymbol{\nu}, \boldsymbol{\eta} \rangle_{\mathcal{L}_{\mathcal{V}}^2(\Omega)} = \int_0^1 \langle \boldsymbol{\nu}(t, \cdot), \boldsymbol{\eta}(t, \cdot) \rangle_{\mathcal{V}} dt \quad \text{for } \boldsymbol{\nu}, \boldsymbol{\eta} \in \mathcal{L}_{\mathcal{V}}^2(\Omega).$$

*Remark 1.* A useful case is when  $\mathcal{V}$  is a reproducing kernel Hilbert space (RKHS) with a symmetric and positive-definite reproducing kernel. Then  $\mathcal{V}$  is an admissible Hilbert space [11]. In the rest of the paper, the space of vector fields is selected as an admissible RKHS for the advantages of sufficient smoothness and fast computability [17].

Furthermore, a flow of diffeomorphisms can be generated via an admissible velocity field, which is stated as the following theorem.

**Theorem 1** ([60, 11]). Let  $\mathcal{V}$  be an admissible Hilbert space and  $\boldsymbol{\nu} \in \mathcal{L}_{\mathcal{V}}^2(\Omega)$  be a velocity field. Then the ODE in (11) admits a unique solution  $\phi^{\boldsymbol{\nu}} \in \mathcal{C}_0^1([0, 1] \times \Omega, \Omega)$ , such that for  $t \in [0, 1]$ , the mapping  $\phi_t^{\boldsymbol{\nu}} : \Omega \rightarrow \Omega$  is a  $\mathcal{C}^1$ -diffeomorphism on  $\Omega$ .

Let us define

$$\mathcal{G}_{\mathcal{V}} := \left\{ \phi : \phi = \phi_{0,1}^{\nu} \text{ for some } \nu \in \mathcal{L}_{\mathcal{V}}^2(\Omega) \right\}, \quad (13)$$

where

$$\phi_{s,t}^{\nu} := \phi_t^{\nu} \circ (\phi_s^{\nu})^{-1} \quad \text{for } 0 \leq t, s \leq 1 \quad (14)$$

and  $\phi_t^{\nu}$  denotes the solution to the ODE in (11) with given  $\nu \in \mathcal{L}_{\mathcal{V}}^2(\Omega)$ . For  $\phi_0^{\nu} = \text{Id}$ , by (14) we know

$$\phi_t^{\nu} = \phi_{0,t}^{\nu}, \quad (\phi_t^{\nu})^{-1} = \phi_{t,0}^{\nu}. \quad (15)$$

Next several important properties about  $\mathcal{G}_{\mathcal{V}}$  are stated as follows.

**Theorem 2** ([60, 11]). *Let  $\mathcal{V}$  be an admissible Hilbert space,  $\mathcal{G}_{\mathcal{V}}$  be defined in (13), and  $d_{\mathcal{G}_{\mathcal{V}}} : \mathcal{G}_{\mathcal{V}} \times \mathcal{G}_{\mathcal{V}} \rightarrow \mathbb{R}_+$  be defined as*

$$d_{\mathcal{G}_{\mathcal{V}}}(\phi, \psi) := \inf_{\substack{\nu \in \mathcal{L}_{\mathcal{V}}^2(\Omega) \\ \psi = \phi \circ \phi_{0,1}^{\nu}}} \|\nu\|_{\mathcal{L}_{\mathcal{V}}^2(\Omega)} \quad \text{for } \phi, \psi \in \mathcal{G}_{\mathcal{V}}. \quad (16)$$

*Then  $\mathcal{G}_{\mathcal{V}}$  is a group for the composition of functions, and  $\mathcal{G}_{\mathcal{V}}$  is a complete metric space under the metric  $d_{\mathcal{G}_{\mathcal{V}}}$ . For each  $\phi, \psi \in \mathcal{G}_{\mathcal{V}}$ , there exists  $\nu \in \mathcal{L}_{\mathcal{V}}^2(\Omega)$  satisfying  $\psi = \phi \circ \phi_{0,1}^{\nu}$ , i.e.,  $d_{\mathcal{G}_{\mathcal{V}}}(\phi, \psi) = \|\nu\|_{\mathcal{L}_{\mathcal{V}}^2(\Omega)}$ .*

This distance can then be used as a regularization term for image registration via the following LDDMM formulation:

$$\min_{\phi \in \mathcal{G}_{\mathcal{V}}} \|\phi \cdot I_0 - I_1\|_{\mathcal{L}^2(\Omega)}^2 + \mu d_{\mathcal{G}_{\mathcal{V}}}^2(\text{Id}, \phi), \quad (17)$$

where  $I_0, I_1 \in \mathcal{L}^2(\Omega)$  are two given images, and  $\mu$  is a nonnegative regularization parameter.

The minimum in (16) is reached and then it is shown in [60, Lemma 11.3] that the previous formulation is equivalent to the following variational model, with a regularization term defined on velocity fields instead of diffeomorphisms:

$$\begin{aligned} \min_{\nu \in \mathcal{L}_{\mathcal{V}}^2(\Omega)} & \|\phi_{0,1}^{\nu} \cdot I_0 - I_1\|_{\mathcal{L}^2(\Omega)}^2 + \mu \int_0^1 \|\nu(t, \cdot)\|_{\mathcal{V}}^2 dt \\ \text{s.t. } & \phi_{0,1}^{\nu} \text{ solves ODE (11) at time } t = 1. \end{aligned} \quad (18)$$

Hence, the regularization term for image registration by LDDMM is formulated as

$$\mathcal{R}(\phi) := d_{\mathcal{G}_{\mathcal{V}}}^2(\text{Id}, \phi) = \int_0^1 \|\nu(t, \cdot)\|_{\mathcal{V}}^2 dt, \quad (19)$$

where the above  $\nu$  is an existing minimum for  $d_{\mathcal{G}_{\mathcal{V}}}(\text{Id}, \phi) = \|\nu\|_{\mathcal{L}_{\mathcal{V}}^2(\Omega)}$  such that  $\nu \in \mathcal{L}_{\mathcal{V}}^2(\Omega)$  satisfying  $\phi = \text{Id} \circ \phi_{0,1}^{\nu}$  (see theorem 2).

## 3.2 Spatiotemporal reconstruction with LDDMM

We assume that the temporal deformation  $\phi_t^{\nu}$  in (6) is generated by the flow equation (11) as in LDDMM. According to theorem 1, the generated flow  $\phi_t^{\nu}$  is diffeomorphism on  $\Omega$  if the velocity field  $\nu \in \mathcal{L}_{\mathcal{V}}^2(\Omega)$ . Consequently, combining

theorem 2 with (19) implies that the shape regularization  $\mathcal{R}_2$  for the temporal deformation  $\phi_t^\nu$  in (6) can be designed as

$$\mathcal{R}_2(\phi_t^\nu) := \int_0^t \|\nu(\tau, \cdot)\|_{\mathcal{V}}^2 d\tau. \quad (20)$$

Note that by theorem 2, the above  $\nu$  is also a minimum for  $d_{\mathcal{G}_\nu}(\text{Id}, \phi_1^\nu) = \|\nu\|_{\mathcal{L}_\nu^2(\Omega)}$ .

Using (15), we have  $\mathcal{R}_2(\phi_t^\nu) = \mathcal{R}_2(\phi_{0,t}^\nu)$ . Considering the general framework in section 2.3, as a special form of (6), the new variational model for joint image reconstruction and motion estimation for spatiotemporal imaging becomes

$$\begin{aligned} \min_{\substack{I \in \mathcal{X} \\ \nu \in \mathcal{L}_\nu^2(\Omega)}} \int_0^1 \left[ \mathcal{D}(\mathcal{T}_t(\phi_{0,t}^\nu, I), g(t, \cdot)) + \mu_2 \int_0^t \|\nu(\tau, \cdot)\|_{\mathcal{V}}^2 d\tau \right] dt + \mu_1 \mathcal{R}_1(I) \\ \text{s.t. } \phi_{0,t}^\nu \text{ solves ODE (11)}. \end{aligned} \quad (21)$$

By simply changing the order of integration for the second term in (21), we obtain the equivalent formulation:

$$\begin{aligned} \min_{\substack{I \in \mathcal{X} \\ \nu \in \mathcal{L}_\nu^2(\Omega)}} \int_0^1 \left[ \mathcal{D}(\mathcal{T}_t(\phi_{0,t}^\nu, I), g(t, \cdot)) + \mu_2(1-t) \|\nu(t, \cdot)\|_{\mathcal{V}}^2 \right] dt + \mu_1 \mathcal{R}_1(I) \\ \text{s.t. } \phi_{0,t}^\nu \text{ solves ODE (11)}. \end{aligned} \quad (22)$$

The model (21) is termed *time-continuous version* of the proposed model. Furthermore, the above model can be restated as partial differential equation (PDE)-constrained optimal control formulation, which is given in the following theorem.

**Theorem 3.** Let  $I \in \mathcal{X}$  and  $f: [0, 1] \times \Omega \rightarrow \mathbb{R}$  be defined as

$$f(t, \cdot) := \phi_{0,t}^\nu \cdot I \quad \text{for } 0 \leq t \leq 1, \quad (23)$$

where  $\phi_{0,t}^\nu$  is a diffeomorphism on  $\Omega$  given by (14). Assume furthermore that  $f(t, \cdot) \in \mathcal{X}$ , and  $\mathcal{X}$  is a sufficiently smooth space. Then, (21) with the group action given by geometric deformation in (4) is equivalent to

$$\begin{aligned} \min_{\substack{f(t, \cdot) \in \mathcal{X} \\ \nu \in \mathcal{L}_\nu^2(\Omega)}} \int_0^1 \left[ \mathcal{D}(\mathcal{T}_t(f(t, \cdot)), g(t, \cdot)) + \mu_2 \int_0^t \|\nu(\tau, \cdot)\|_{\mathcal{V}}^2 d\tau \right] dt + \mu_1 \mathcal{R}_1(f(0, \cdot)) \\ \text{s.t. } \partial_t f(t, \cdot) + \langle \nabla f(t, \cdot), \nu(t, \cdot) \rangle_{\mathbb{R}^n} = 0. \end{aligned} \quad (24)$$

With the group action given by mass-preserving deformation in (5), then (21) is equivalent to

$$\begin{aligned} \min_{\substack{f(t, \cdot) \in \mathcal{X} \\ \nu \in \mathcal{L}_\nu^2(\Omega)}} \int_0^1 \left[ \mathcal{D}(\mathcal{T}_t(f(t, \cdot)), g(t, \cdot)) + \mu_2 \int_0^t \|\nu(\tau, \cdot)\|_{\mathcal{V}}^2 d\tau \right] dt + \mu_1 \mathcal{R}_1(f(0, \cdot)) \\ \text{s.t. } \partial_t f(t, \cdot) + \nabla \cdot (f(t, \cdot) \nu(t, \cdot)) = 0. \end{aligned} \quad (25)$$



*Proof.* First we consider the geometric deformation in (4), i.e., (23) reads as

$$f(t, \cdot) = I \circ (\phi_{0,t}^\nu)^{-1} \quad \text{for } 0 \leq t \leq 1. \quad (26)$$

Obviously,  $f(0, \cdot) = I$  and  $f(1, \cdot) = I \circ (\phi_{0,1}^\nu)^{-1}$ . Furthermore, applying the variable transformation for (26), we get

$$f(t, \phi_{0,t}^\nu) = I \quad \text{for } 0 \leq t \leq 1. \quad (27)$$

Differentiating (27) w.r.t. time  $t$  leads to

$$\partial_t f(t, \phi_{0,t}^\nu) + \langle \nabla f(t, \phi_{0,t}^\nu), \nu(t, \phi_{0,t}^\nu) \rangle_{\mathbb{R}^n} = 0.$$

Then the PDE constraint in (24) is obtained. Hence a solution to (21) generates a solution to (24).

We now consider the reverse implication, i.e., demonstrate that a solution to (24) also solves (21). Suppose that  $f$  and  $\nu$  solve (24). Define the diffeomorphism  $\psi_t$  that solves the ODE (11) with the above given  $\nu$ . Since  $f$  satisfies PDE constraint in (24), considering  $t \mapsto f(t, \psi_t)$ , we have

$$\frac{d}{dt} f(t, \psi_t) = \partial_t f(t, \psi_t) + \langle \nabla f(t, \psi_t), \nu(t, \psi_t) \rangle_{\mathbb{R}^n} = 0.$$

Hence,  $t \mapsto f(t, \psi_t)$  is constant so in particular we have

$$f(t, \psi_t) \equiv f(0, \psi_0) = f(0, \cdot).$$

Let  $f(0, \cdot)$  be the template  $I$  and  $\psi_t$  be  $\phi_{0,t}^\nu$ . Then  $f(t, \cdot) = I \circ (\phi_{0,t}^\nu)^{-1}$ . Hence a solution to (24) also produces a solution to (21).

Using a mass-preserving deformation (5) as group action in (23) results in

$$f(t, \cdot) = |D((\phi_{0,t}^\nu)^{-1})| I \circ (\phi_{0,t}^\nu)^{-1} \quad \text{for } 0 \leq t \leq 1. \quad (28)$$

We then get that  $f(0, \cdot) = I$  and  $f(1, \cdot) = |D((\phi_{0,1}^\nu)^{-1})| I \circ (\phi_{0,1}^\nu)^{-1}$ . The symmetry of the mass-preserving property furthermore yields

$$|D(\phi_{0,t}^\nu)| f(t, \cdot) \circ \phi_{0,t}^\nu = I \quad \text{for } 0 \leq t \leq 1. \quad (29)$$

Finally, differentiating (29) w.r.t.  $t$  leads to the constraint in (25). Hence, a minimizer of (21) with the group action given by (5) is also a minimizer of (25). Similar to the case of geometric deformation, it is not difficult to prove the reverse implication.  $\square$

The above equivalent formulation makes it easier for us to compare our proposed approach against PDE based ones, such as those based on optical flow [13]. More details are provided in section 3.3.

### 3.3 Comparison with existing approaches

In this section, the mathematical comparison will be made among the proposed model (21) and several existing approaches (i.e., optical flow based model, diffeomorphic motion models).

### 3.3.1 Comparison to optical flow based model

Recently, an optical flow based variational model was proposed for joint motion estimation and image reconstruction in spatiotemporal imaging, which is called joint TV-TV optical flow model in [13]. The approach is formulated as a PDE-constrained optimal control problem, so we can compare it to our approach using the reformulation in (24).

Since the optical flow based model is set up in terms of the brightness constancy equation, this points to using the geometric deformation in (4) as a group action in (23), i.e., we assume (26) holds. The optical flow based approach reads as

$$\begin{aligned} \min_{\substack{f(t, \cdot) \in \mathcal{X} \\ \boldsymbol{\nu}(t, \cdot) \in BV(\Omega)}} \int_0^1 & \left[ \mathcal{D}(\mathcal{T}_t(f(t, \cdot)), g(t, \cdot)) + \mu_1 \mathcal{R}_1(f(t, \cdot)) + \mu_2 \|\boldsymbol{\nu}(t, \cdot)\|_{BV} \right] dt \\ \text{s.t. } & \partial_t f(t, \cdot) + \langle \nabla f(t, \cdot), \boldsymbol{\nu}(t, \cdot) \rangle_{\mathbb{R}^n} = 0, \end{aligned} \quad (30)$$

where  $\|\cdot\|_{BV}$  is the TV semi-norm in the space of functions with bounded variation (BV)

$$BV(\Omega) := \left\{ u \in L^1(\Omega) : \|u\|_{BV} = \sup_{\varphi \in \mathcal{C}_0^1(\Omega, \mathbb{R}^n), \|\varphi\|_\infty \leq 1} \int_\Omega u \operatorname{div} \varphi dx < \infty \right\}.$$

Note that  $\|\boldsymbol{\nu}(t, \cdot)\|_{BV}$  denotes the sum of the TV semi-norm of all the elements in  $\boldsymbol{\nu}(t, \cdot)$  [1].

It is easy to see that the constraints in (24) and (30) are equivalent. Hence, the geometric deformation is equivalent to using an the optical flow constraint or the brightness constancy equation [13].

By comparison, the primary distinction between (24) and (30) relates to the selection of the regularization term w.r.t. vector field  $\boldsymbol{\nu}(t, \cdot)$ . In model (30), its selection is TV semi-norm. Hence, the space of vector fields is included in  $BV(\Omega)$ , which allows for a vector field that is a piecewise-constant vector-valued function distributed on  $\Omega$ . By contrast in model (24), the space of vector fields is included in an admissible Hilbert space. Hence, the vector field is a sufficiently smooth vector-valued function distributed on  $\Omega$ . This guarantees an elastic diffeomorphic deformation, which is close to the physical mechanism to some extent [29, 14].

In addition to the above, both approaches also differ in the selection of regularization term  $\mathcal{R}_1$ . In (24) one only poses restriction on the initial image  $f(0, \cdot)$ , whereas in (30) the whole time trajectory  $t \mapsto f(t, \cdot)$  is regularized. Hence, (24) has a simpler structure which is also beneficial in implementation.

### 3.3.2 Compared with diffeomorphic motion models

To characterize the optimality conditions for (21) we introduce the notation

$$\mathcal{D}_{g_t}(f) := \mathcal{D}(\mathcal{T}_t(f), g(t, \cdot)) \quad (31)$$

for  $f \in \mathcal{X}$  with given  $g(t, \cdot) \in \mathcal{Y}$ . By theorem 4 in appendix A, the optimal velocity field in (21) satisfies

$$\boldsymbol{\nu}(t, \cdot) = \frac{1}{2\mu_2(1-t)} \int_t^1 \mathcal{K} \left( \nabla(\phi_{0,t}^\nu \cdot I) |D(\phi_{t,\tau}^\nu)| \nabla \mathcal{D}_{g_\tau}(\phi_{0,\tau}^\nu \cdot I)(\phi_{t,\tau}^\nu) \right) d\tau \quad (32)$$

for  $0 \leq t < 1$ . The above optimal velocity field can be seen as the average of the integrand w.r.t. the time integral. The  $\boldsymbol{\nu}(1, \cdot)$  is well-defined at  $t = 1$  as

$$\boldsymbol{\nu}(1, \cdot) = \frac{1}{2\mu_2} \mathcal{K}(\nabla(\phi_{0,1}^\nu \cdot I) \nabla \mathcal{D}_{g_1}(\phi_{0,1}^\nu \cdot I)). \quad (33)$$

By (76) and (77) we get at  $t = 0$  that

$$\boldsymbol{\nu}(0, \cdot) = \frac{1}{2\mu_2} \mathcal{K} \left( \nabla I \int_0^1 |D(\phi_{0,t}^\nu)| \nabla \mathcal{D}_{g_t}(\phi_{0,t}^\nu \cdot I)(\phi_{0,t}^\nu) dt \right). \quad (34)$$

Note that the optimal velocity field in (21) is *averagely distributed w.r.t. time  $t$* , and also *non-vanishing neither on the initial nor on the end time point*.

A diffeomorphic motion model was proposed for 4D CT image reconstruction in [32] that is based on the LDDMM growth model [30]. The related time-continuous model reads as

$$\begin{aligned} \min_{\substack{I \in \mathcal{X} \\ \boldsymbol{\nu} \in \mathcal{L}_{\mathcal{Y}}^2(\Omega)}} \int_0^1 \left[ \mathcal{D}(\mathcal{T}_t(\phi_{0,t}^\nu \cdot I), g(t, \cdot)) + \mu_2 \|\boldsymbol{\nu}(t, \cdot)\|_{\mathcal{Y}}^2 \right] dt \\ \text{s.t. } \phi_{0,t}^\nu \text{ solves ODE (11).} \end{aligned} \quad (35)$$

Compared to (21), the above approach neglects the regularization term  $\mathcal{R}_1$  absolutely. Another difference relates to the selection on the shape regularization  $\mathcal{R}_2$ . In (35), the shape regularization is a uniformly weighted term on  $\|\boldsymbol{\nu}(t, \cdot)\|_{\mathcal{Y}}^2$ . In contrast, that is a non-uniformly weighted term in (21) (see (22) for more clear), which fulfils more weights on the previous time.

*Remark 2.* Note that in (21), we regularize the velocity field more at the beginning, and which is relevant because the template is selected at the initial time, and the more beginning of the velocity field, the more influence on the whole geodesic trajectory.

For further comparison, by theorem 4, it is easy to see that the  $\mathcal{L}_{\mathcal{Y}}^2(\Omega)$ -norm minimizer of (35) w.r.t. variations of the velocity field satisfies

$$\boldsymbol{\nu}(t, \cdot) = \frac{1}{2\mu_2} \int_t^1 \mathcal{K} \left( \nabla(\phi_{0,t}^\nu \cdot I) |D(\phi_{t,\tau}^\nu)| \nabla \mathcal{D}_{g_\tau}(\phi_{0,\tau}^\nu \cdot I)(\phi_{t,\tau}^\nu) \right) d\tau \quad (36)$$

for  $0 \leq t \leq 1$  and  $\mu_2 > 0$ . In addition, the minimizer w.r.t. variations of the template satisfies

$$\int_0^1 |D(\phi_{0,t}^\nu)| \nabla \mathcal{D}_{g_t}(\phi_{0,t}^\nu \cdot I)(\phi_{0,t}^\nu) dt = 0. \quad (37)$$

Combining (36) and (37), we immediately have

$$\boldsymbol{\nu}(0, \cdot) = \boldsymbol{\nu}(1, \cdot) = 0.$$

Clearly, the optimal velocity field that minimizes (35) is *vanishing both on the initial and end time points*. It is not difficult to see from (36) that the optimal velocity field is *not averagely distributed w.r.t. time  $t$* .

On the other hand, the following model can be seen as another diffeomorphic motion model.

$$\begin{aligned} \min_{\substack{I \in \mathcal{X} \\ \boldsymbol{\nu} \in \mathcal{L}_{\mathcal{V}}^2(\Omega)}} \int_0^1 \left[ \mathcal{D}(\mathcal{T}_t(\phi_{0,t}^{\boldsymbol{\nu}}, I), g(t, \cdot)) + \mu_1 \mathcal{R}_1(\phi_{0,t}^{\boldsymbol{\nu}}, I) + \mu_2 \int_0^t \|\boldsymbol{\nu}(\tau, \cdot)\|_{\mathcal{V}}^2 d\tau \right] dt \\ \text{s.t. } \phi_{0,t}^{\boldsymbol{\nu}} \text{ solves ODE (11).} \end{aligned} \quad (38)$$

We consider the regularization term on the whole  $\phi_t \cdot I$  instead of only on  $I$  in (6). By theorem 4, its optimal velocity field for  $0 \leq t < 1$  satisfies

$$\boldsymbol{\nu}(t, \cdot) = \frac{1}{2\mu_2(1-t)} \int_t^1 \mathcal{K}(\nabla(\phi_{0,t}^{\boldsymbol{\nu}}, I) |D(\phi_{t,\tau}^{\boldsymbol{\nu}})| \nabla \mathcal{S}_{g_\tau}(\phi_{0,\tau}^{\boldsymbol{\nu}}, I)(\phi_{t,\tau}^{\boldsymbol{\nu}})) d\tau \quad (39)$$

where with fixed  $g(t, \cdot) \in \mathcal{V}$ ,

$$\mathcal{S}_{g_t}(f) := \mathcal{D}(\mathcal{T}_t(f), g(t, \cdot)) + \mu_1 \mathcal{R}_1(f)$$

for  $f \in \mathcal{X}$ . And its optimal template satisfies

$$\int_0^1 |D(\phi_{0,t}^{\boldsymbol{\nu}})| \nabla \mathcal{S}_{g_t}(\phi_{0,t}^{\boldsymbol{\nu}}, I)(\phi_{0,t}^{\boldsymbol{\nu}}) dt = 0. \quad (40)$$

Evidently, the above optimal velocity field is also a time average of the integrand. Even though  $\boldsymbol{\nu}(1, \cdot)$  is well-defined at  $t = 1$  as

$$\boldsymbol{\nu}(1, \cdot) = \frac{1}{2\mu_2} \mathcal{K}(\nabla(\phi_{0,1}^{\boldsymbol{\nu}}, I) \nabla \mathcal{S}_{g_1}(\phi_{0,1}^{\boldsymbol{\nu}}, I)),$$

by (39) and (40) at  $t = 0$  we have

$$\boldsymbol{\nu}(0, \cdot) = 0.$$

Hence, the optimal velocity field in (38) is *averagely distributed w.r.t. time  $t$* , but *vanishing on the initial time point*.

The above analysis points to several advantages that comes with using (21) over alternative approaches.

## 4 Numerical implementation

Let us first present the time-discretized version of the proposed model.

### 4.1 Time-discretized version

Basically, the data set is gained by gating method in the manner of uniformly discretized time, i.e., based on a uniform partition of  $[0, 1]$  as  $\{t_i\}_{i=0}^N$ , and  $t_i = i/N$  for  $0 \leq i \leq N$ . We refer to this as the gating grid and the time-discretized version of the general spatiotemporal inverse problem in (1) reads as

$$g(t_i, \cdot) = \mathcal{T}_{t_i}(f(t_i, \cdot)) + g_{\text{noise}}(t_i, \cdot). \quad (41)$$

Thus the time-discretized version of (21) becomes

$$\begin{aligned} \min_{\substack{I \in \mathcal{X} \\ \boldsymbol{\nu} \in \mathcal{L}_{\mathcal{V}}^2(\Omega)}} \frac{1}{N} \sum_{i=1}^N \left[ \mathcal{D}(\mathcal{T}_{t_i}(\phi_{0,t_i}^{\boldsymbol{\nu}} \cdot I), g(t_i, \cdot)) + \mu_2 \int_0^{t_i} \|\boldsymbol{\nu}(\tau, \cdot)\|_{\mathcal{V}}^2 d\tau \right] + \mu_1 \mathcal{R}_1(I) \\ \text{s.t. } \phi_{0,t}^{\boldsymbol{\nu}} \text{ solves ODE (11).} \end{aligned} \quad (42)$$

*Remark 3.* The time-discretized version (42) can be also written such that the image in the first gate is the template:

$$\begin{aligned} \min_{\substack{I \in \mathcal{X} \\ \boldsymbol{\nu} \in \mathcal{L}_{\mathcal{V}}^2(\Omega)}} \frac{1}{N+1} \sum_{i=0}^N \left[ \mathcal{D}(\mathcal{T}_{t_i}(\phi_{0,t_i}^{\boldsymbol{\nu}} \cdot I), g(t_i, \cdot)) + \mu_2 \int_0^{t_i} \|\boldsymbol{\nu}(\tau, \cdot)\|_{\mathcal{V}}^2 d\tau \right] + \mu_1 \mathcal{R}_1(I) \\ \text{s.t. } \phi_{0,t}^{\boldsymbol{\nu}} \text{ solves ODE (11).} \end{aligned}$$

Since (42) contains highly coupled arguments, it is difficult to jointly solve for the template  $I$  and the velocity field  $\boldsymbol{\nu}$ . A relaxed method is to compute  $I$  and  $\boldsymbol{\nu}$  in an intertwined manner. More precisely, a fixed velocity field  $\boldsymbol{\nu}$  yields the flow of diffeomorphisms  $\phi_t$  through ODE (11). Hence, the spatiotemporal reconstruction problem (42) reduces to the following modified static image reconstruction problem:

$$\min_{I \in \mathcal{X}} \frac{1}{N} \sum_{i=1}^N \mathcal{D}(\mathcal{T}_{t_i}(\phi_{0,t_i}^{\boldsymbol{\nu}} \cdot I), g(t_i, \cdot)) + \mu_1 \mathcal{R}_1(I). \quad (43)$$

Conversely, if the template  $I$  is fixed then (42) boils down to a sequentially indirect image registration problem where we seek the velocity field  $\boldsymbol{\nu}$  from time-series data that are indirect observations of the target:

$$\begin{aligned} \min_{\boldsymbol{\nu} \in \mathcal{L}_{\mathcal{V}}^2(\Omega)} \frac{1}{N} \sum_{i=1}^N \left[ \mathcal{D}(\mathcal{T}_{t_i}(\phi_{0,t_i}^{\boldsymbol{\nu}} \cdot I), g(t_i, \cdot)) + \mu_2 \int_0^{t_i} \|\boldsymbol{\nu}(\tau, \cdot)\|_{\mathcal{V}}^2 d\tau \right] \\ \text{s.t. } \phi_{0,t}^{\boldsymbol{\nu}} \text{ solves ODE (11).} \end{aligned} \quad (44)$$

We solve (42) by alternately solving for (43) and (44).

If the data fidelity term is designed as the squared  $\mathcal{L}^2$ -norm in (7) and the spatial regularization is selected as the TV functional in (10), then (42) is written as

$$\begin{aligned} \min_{\substack{I \in \mathcal{X} \\ \boldsymbol{\nu} \in \mathcal{L}_{\mathcal{V}}^2(\Omega)}} \frac{1}{N} \sum_{i=1}^N \left[ \|\mathcal{T}_{t_i}(\phi_{0,t_i}^{\boldsymbol{\nu}} \cdot I) - g(t_i, \cdot)\|_2^2 + \mu_2 \int_0^{t_i} \|\boldsymbol{\nu}(\tau, \cdot)\|_{\mathcal{V}}^2 d\tau \right] + \mu_1 \|\nabla I\| \\ \text{s.t. } \phi_{0,t}^{\boldsymbol{\nu}} \text{ solves ODE (11).} \end{aligned} \quad (45)$$

Note that one may of course choose other data fidelity and spatial regularization terms as indicated in section 2.3. Correspondingly, (43) becomes

$$\min_{I \in \mathcal{X}} \mathcal{E}_{\boldsymbol{\nu}}(I) := \frac{1}{N} \sum_{i=1}^N \|\mathcal{T}_{t_i}(\phi_{0,t_i}^{\boldsymbol{\nu}} \cdot I) - g(t_i, \cdot)\|_2^2 + \mu_1 \|\nabla I\|, \quad (46)$$

and (44) reads as

$$\begin{aligned} \min_{\boldsymbol{\nu} \in \mathcal{L}_{\mathcal{V}}^2(\Omega)} \mathcal{E}_I(\boldsymbol{\nu}) &:= \frac{1}{N} \sum_{i=1}^N \left[ \|\mathcal{T}_{t_i}(\phi_{0,t_i}^{\boldsymbol{\nu}} \cdot I) - g(t_i, \cdot)\|_2^2 + \mu_2 \int_0^{t_i} \|\boldsymbol{\nu}(\tau, \cdot)\|_{\mathcal{V}}^2 d\tau \right] \\ \text{s.t. } \phi_{0,t}^{\boldsymbol{\nu}} &\text{ solves the ODE (11),} \end{aligned} \quad (47)$$

where  $\mathcal{E}_{\boldsymbol{\nu}}: \mathcal{X} \rightarrow \mathbb{R}$  and  $\mathcal{E}_I: \mathcal{L}_{\mathcal{V}}^2(\Omega) \rightarrow \mathbb{R}$ . We then solve (45) by alternately solving for (46) and (47), i.e.,

$$\begin{cases} I^{k+1} := \text{solution to (46) with } \boldsymbol{\nu} = \boldsymbol{\nu}^k, \\ \boldsymbol{\nu}^{k+1} := \text{solution to (47) with } I = I^{k+1}. \end{cases} \quad (48)$$

## 4.2 Template reconstruction

Just as in [7, 9, 35, 13], the temporal evolution operator in spatiotemporal imaging can be given by the geometric deformation as  $\phi_{0,t} \cdot I := I \circ \phi_{t,0}^{-1} = I \circ \phi_{0,t}$ . We will henceforth consider this setting. We here describe the steps underlying the implementation for solving the static image reconstruction problem in (46). The resulting gradient descent scheme is summarized in algorithm 1. The resulting template, which is obtained assuming a given velocity field, gives the images in all gates by deforming it under the flow of diffeomorphisms.

The optimization problem in (45) is a non-smooth TV- $\ell_2$  minimization. We modify this non-smooth problem into a smooth one as

$$\min_{I \in \mathcal{X}} \frac{1}{N} \sum_{i=1}^N \|\mathcal{T}_{t_i}(I \circ \phi_{t_i,0}^{\boldsymbol{\nu}}) - g(t_i, \cdot)\|_2^2 + \mu_1 \int_{\Omega} |\nabla I(x)|_{1,\epsilon} dx, \quad (49)$$

where  $|\nabla I(x)|_{1,\epsilon} = \sqrt{\sum_i (\partial_i I(x))^2 + \epsilon}$  with  $\epsilon > 0$  small, e.g.,  $\epsilon = 10^{-12}$ . This is a frequently used modification for TV regularization in image reconstruction [49, 18, 16]. Then (49) can be solved by the following gradient descent scheme:

$$\begin{aligned} I^{k+1} = I^k - \alpha^k &\left( \frac{2}{N} \sum_{i=1}^N |D(\phi_{0,t_i}^{\boldsymbol{\nu}})| \mathcal{T}_{t_i}^* \left( \mathcal{T}_{t_i}(I^k \circ \phi_{t_i,0}^{\boldsymbol{\nu}}) - g(t_i, \cdot) \right) (\phi_{0,t_i}^{\boldsymbol{\nu}}) \right. \\ &\left. + \mu_1 \nabla^* \left( \frac{\nabla I^k}{|\nabla I^k|_{1,\epsilon}} \right) \right) \end{aligned} \quad (50)$$

with  $\alpha^k$  the stepsize for the  $k$ -th iteration, where  $\mathcal{T}$  is assumed to be linear, and  $\mathcal{T}^*$  denotes its adjoint operator.

Note that several convex optimization techniques for solving non-smooth problems in static image reconstruction, such as the algorithms in [48, 19, 41, 20, 4] and references therein, can be used to solve (46) without modification. Basically such kind of methods need to introduce more auxiliary variables or parameters than the above algorithm. To optimize the whole problem (45) efficiently, we employ the iterative scheme (50) to solve this subproblem.

#### 4.2.1 Computing diffeomorphic deformations

Updating  $I^{k+1}$  requires computing diffeomorphic deformations  $\phi_{t_i,0}^\nu$  and  $\phi_{0,t_i}^\nu$  for  $1 \leq i \leq N$ .

By definition,  $\phi_{s,t}^\nu$  solves the flow equation

$$\begin{cases} \partial_t \varphi(t, x) = \nu(t, \varphi(t, x)) \\ \varphi(s, x) = x \end{cases} \quad \text{for } x \in \Omega \text{ and } 0 \leq s, t \leq 1, \quad (51)$$

where  $s$  is a fixed time point. Integrating w.r.t. time  $t$  in (51) yields

$$\phi_{s,t}^\nu = \text{Id} + \int_s^t \nu(\tau, \phi_{s,\tau}^\nu) d\tau \quad \text{for } 0 \leq t \leq 1. \quad (52)$$

The time interval  $[0, 1]$  is subdivided uniformly into  $MN$  parts thereby forming a discretized time grid that is given as  $\tau_j = j/(MN)$  for  $j = 0, 1, \dots, MN$ . Evidently,  $\tau_{iM} = t_i$  for  $i = 0, 1, \dots, N$ , so each subinterval  $[t_i, t_{i+1}]$  is segmented into  $M$  even parts. The  $M$  is named as a factor of discretized time degree. If  $M = 1$ , then  $\tau_i = t_i$ , namely, the discretized time grid is consistent with the gating grid. Needs to be pointed out is that the different subintervals of gating grid can be discretized adaptively according to the degree of motions.

Within a short-time interval one can approximate the diffeomorphic deformation with linearized deformations [42]. More precisely, let  $s = \tau_j$ ,  $t = \tau_{j-1}$  and  $\tau_{j+1}$  in (52), then the expressions for small deformations  $\phi_{\tau_i, \tau_{i-1}}^\nu$  and  $\phi_{\tau_i, \tau_{i+1}}^\nu$  can be approximated by

$$\phi_{\tau_j, \tau_{j-1}}^\nu \approx \text{Id} - \frac{1}{MN} \nu(\tau_j, \cdot), \quad (53)$$

and

$$\phi_{\tau_j, \tau_{j+1}}^\nu \approx \text{Id} + \frac{1}{MN} \nu(\tau_j, \cdot). \quad (54)$$

Moreover, (14) implies that  $\phi_{\tau_j, 0}^\nu = \phi_{\tau_{j-1}, 0}^\nu \circ \phi_{\tau_j, \tau_{j-1}}^\nu$ , which combined with (53) yields

$$\phi_{\tau_j, 0}^\nu \approx \phi_{\tau_{j-1}, 0}^\nu \circ \left( \text{Id} - \frac{1}{MN} \nu(\tau_j, \cdot) \right) \quad \text{for } j = 1, 2, \dots, MN. \quad (55)$$

Next, (55) yields the following estimate for  $I \circ \phi_{\tau_j, 0}^\nu$ :

$$I \circ \phi_{\tau_j, 0}^\nu \approx (I \circ \phi_{\tau_{j-1}, 0}^\nu) \circ \left( \text{Id} - \frac{1}{MN} \nu(\tau_j, \cdot) \right) \quad (56)$$

for  $j = 1, 2, \dots, MN$  and with  $I \circ \phi_{\tau_0, 0}^\nu = I$ . Similarly, (14) also implies  $\phi_{\tau_j, t_i}^\nu = \phi_{\tau_{j+1}, t_i}^\nu \circ \phi_{\tau_j, \tau_{j+1}}^\nu$  for  $i \geq 1$ , which combined with (54) gives the following approximation:

$$\phi_{\tau_j, t_i}^\nu \approx \phi_{\tau_{j+1}, t_i}^\nu \circ \left( \text{Id} + \frac{1}{MN} \nu(\tau_j, \cdot) \right) \quad (57)$$

for  $j = iM - 1, iM - 2, \dots, 0$  and with  $\phi_{t_i, t_i}^\nu = \text{Id}$ .

To summarize, the deformation between two images of adjacent points of discretized time grid is approximately represented as a linearized deformation.

### 4.2.2 Computing mass-preserving deformations

The gradient of the data fidelity term involves the type of mass-preserving deformation in (5) as

$$|D(\phi_{0,t_i}^\nu)| \mathcal{T}_{t_i}^* \left( \mathcal{T}_{t_i}(I \circ \phi_{t_i,0}^\nu) - g(t_i, \cdot) \right) \circ \phi_{0,t_i}^\nu \quad \text{for } i \geq 1.$$

Starting with the Jacobian determinant, by (57) we get

$$|D(\phi_{\tau_j,t_i}^\nu)| \approx \left( 1 + \frac{1}{MN} \operatorname{div} \nu(\tau_j, \cdot) \right) |D(\phi_{\tau_{j+1},t_i}^\nu)| \circ \left( \operatorname{Id} + \frac{1}{MN} \nu(\tau_j, \cdot) \right) \quad (58)$$

for  $j = iM - 1, iM - 2, \dots, 0$  and where  $|D(\phi_{t_i,t_i}^\nu)| = 1$ . Next, (57) also yields the following approximation:

$$\begin{aligned} \mathcal{T}_{t_i}^* \left( \mathcal{T}_{t_i}(I \circ \phi_{t_i,0}^\nu) - g(t_i, \cdot) \right) \circ \phi_{\tau_j,t_i}^\nu \\ \approx \mathcal{T}_{t_i}^* \left( \mathcal{T}_{t_i}(I \circ \phi_{t_i,0}^\nu) - g(t_i, \cdot) \right) \circ \phi_{\tau_{j+1},t_i}^\nu \circ \left( \operatorname{Id} + \frac{1}{MN} \nu(\tau_j, \cdot) \right) \end{aligned} \quad (59)$$

for  $j = iM - 1, iM - 2, \dots, 0$ . For simplicity, let

$$\eta_{\tau,t}^{I,\nu} = |D(\phi_{\tau,t}^\nu)| \mathcal{T}_t^* \left( \mathcal{T}_t(I \circ \phi_{t,0}^\nu) - g(t, \cdot) \right) \circ \phi_{\tau,t}^\nu. \quad (60)$$

Then multiplying (58) by (59), and using (60),  $\eta_{0,t_i}^{I,\nu}$  for  $i \geq 1$  is computed by

$$\eta_{\tau_j,t_i}^{I,\nu} \approx \left( 1 + \frac{1}{MN} \operatorname{div} \nu(\tau_j, \cdot) \right) \eta_{\tau_{j+1},t_i}^{I,\nu} \circ \left( \operatorname{Id} + \frac{1}{MN} \nu(\tau_j, \cdot) \right) \quad (61)$$

for  $j = iM - 1, iM - 2, \dots, 0$  with  $\eta_{t_i,t_i}^{I,\nu} = \mathcal{T}_{t_i}^* \left( \mathcal{T}_{t_i}(I \circ \phi_{t_i,0}^\nu) - g(t_i, \cdot) \right)$ .

Based on the above derivations, the concrete implementation is given as the gradient descent scheme in algorithm 1.

## 4.3 Velocity field estimation

The aim here is to provide an algorithm for solving (47), which is sequentially indirect image registration. We will use a gradient descent scheme of the form

$$\nu^{k+1} = \nu^k - \beta^k \nabla \mathcal{E}_I(\nu^k). \quad (62)$$

Here  $\mathcal{E}_I: \mathcal{L}_{\mathcal{T}}^2(\Omega) \rightarrow \mathbb{R}$  is the objective functional in (47),  $\beta^k$  is the step-size in the  $k$ -th iteration, and  $\nabla \mathcal{E}_I(\nu)$  is calculated by (80).

The central issue is the computation of  $\nabla \mathcal{E}_I$  and the final algorithm for the gradient descent scheme (62) is given in algorithm 2.

### 4.3.1 Computing $\nabla \mathcal{E}_I$

Let us first introduce notations:

$$h_{\tau,t}^{I,\nu} := \begin{cases} \eta_{\tau,t}^{I,\nu}, & 0 \leq \tau \leq t \leq 1, \\ 0, & t < \tau, \end{cases} \quad (63)$$



---

**Algorithm 1** Gradient descent scheme for minimizing  $\mathcal{E}_\nu(I)$  in (46)

---

- 1: *Initialize:*
- 2:  $k \leftarrow 0$ .
- 3:  $t_i \leftarrow \frac{i}{N}$  for  $i = 0, 1, \dots, N$ .
- 4:  $\tau_j \leftarrow \frac{j}{MN}$  for  $j = 0, 1, \dots, MN$ .
- 5: Given  $\nu$ .
- 6:  $I^k \leftarrow I^0$ . Here  $I^0$  is a given initial template.
- 7: Spatial regularization parameter  $\mu_1 > 0$ .
- 8: Error tolerance  $\epsilon_I > 0$ , stepsize  $\alpha^k = \alpha > 0$ , and iteration number  $K_I > 0$ .
- 9: *Loop:*
- 10: Compute  $I^k \circ \phi_{\tau_j, 0}^\nu$  for  $1 \leq j \leq MN$  by

$$I^k \circ \phi_{\tau_j, 0}^\nu \leftarrow (I^k \circ \phi_{\tau_{j-1}, 0}^\nu) \circ \left( \text{Id} - \frac{1}{MN} \nu(\tau_j, \cdot) \right)$$

with  $I^k \circ \phi_{0, 0}^\nu = I^k$ .

- 11: Update  $\eta_{t_i, t_i}^{I^k, \nu}$  for  $1 \leq i \leq N$  by

$$\eta_{t_i, t_i}^{I^k, \nu} \leftarrow \mathcal{T}_{t_i}^* (\mathcal{T}_{t_i} (I^k \circ \phi_{t_i, 0}^\nu) - g(t_i, \cdot))$$

- 12: Compute  $\eta_{0, t_i}^{I^k, \nu}$  for  $1 \leq i \leq N$  by

$$\eta_{\tau_j, t_i}^{I^k, \nu} \leftarrow \left( 1 + \frac{1}{MN} \text{div } \nu(\tau_j, \cdot) \right) \eta_{\tau_{j+1}, t_i}^{I^k, \nu} \circ \left( \text{Id} + \frac{1}{MN} \nu(\tau_j, \cdot) \right)$$

for  $j = iM - 1, iM - 2, \dots, 0$ .

- 13: Evaluate  $I^{k+1}$  by

$$I^{k+1} \leftarrow I^k - \alpha \left( \frac{2}{N} \sum_{i=1}^N \eta_{0, t_i}^{I^k, \nu} + \mu_1 \nabla^* \left( \frac{\nabla I^k}{|\nabla I^k|_{1, \epsilon}} \right) \right).$$

- 14: **If**  $|I^{k+1} - I^k| > \epsilon_I$  and  $k < K_I$ , then  $k \leftarrow k + 1$ , **goto** *Loop*.
  - 15: **Output**  $I^{k+1}$ .
-

and

$$\boldsymbol{\nu}_{\tau,t} := \begin{cases} \boldsymbol{\nu}(\tau, \cdot), & 0 \leq \tau \leq t \leq 1, \\ 0, & t < \tau. \end{cases} \quad (64)$$

Theorem 5 gives an expression for  $\nabla \mathcal{E}_I$  where the kernel function  $\mathbf{K}: \Omega \times \Omega \rightarrow \mathbb{M}_+^{n \times n}$  is evaluated on points that do not move as iteration proceeds. By choosing a translation invariant kernel and points on a regular grid in  $\Omega$ , we can use FFT-based convolution scheme to efficiently evaluate the velocity field at each iteration. This is computationally more feasible than letting the kernel depend on points that move in time as in the shooting method [38, 57].

In what follows, we write out the explicit derivations for computing  $\nabla \mathcal{E}_I(\boldsymbol{\nu})$ . As derived in section 4.2.1,  $I \circ \phi_{\tau_j,0}^\nu$  can be approximated by (56). The key step is now to update  $h_{\tau_j,t_i}^{I,\nu}$  for  $\{i : t_i \geq \tau_j\}$  in (80). We know, by (63),

$$h_{\tau_j,t_i}^{I,\nu} = \eta_{\tau_j,t_i}^{I,\nu} \quad \text{for } t_i \geq \tau_j. \quad (65)$$

Using (61) for  $1 \leq i \leq N$  allows us to compute  $h_{\tau_j,t_i}^{I,\nu}$  by

$$h_{\tau_j,t_i}^{I,\nu} \approx \left(1 + \frac{1}{MN} \operatorname{div} \boldsymbol{\nu}(\tau_j, \cdot)\right) h_{\tau_{j+1},t_i}^{I,\nu} \circ \left(\operatorname{Id} + \frac{1}{MN} \boldsymbol{\nu}(\tau_j, \cdot)\right) \quad (66)$$

for  $j = iM - 1, iM - 2, \dots, 0$  and with  $h_{t_i,t_i}^{I,\nu} = \mathcal{T}_{t_i}^* \left( \mathcal{T}_{t_i}(I \circ \phi_{t_i,0}^\nu) - g(t_i, \cdot) \right)$ . Hence, at  $t = \tau_j$ , by (80) we get

$$\begin{aligned} & \nabla \mathcal{E}_I(\boldsymbol{\nu})(\tau_j, x) \\ &= -\frac{2}{N} \sum_{\{i \geq 1 : t_i \geq \tau_j\}} \left[ \int_{\Omega} \mathbf{K}(x, y) \nabla (I \circ \phi_{\tau_j,0}^\nu)(y) h_{\tau_j,t_i}^{I,\nu}(y) dy - \mu_2 \boldsymbol{\nu}(\tau_j, x) \right] \end{aligned} \quad (67)$$

for  $0 \leq j \leq MN$  and  $x \in \Omega$ . In particular, for  $j = MN$  (i.e.,  $\tau_j = 1$ ) we have

$$\nabla \mathcal{E}_I(\boldsymbol{\nu})(1, x) = -\frac{2}{N} \left[ \int_{\Omega} \mathbf{K}(x, y) \nabla (I \circ \phi_{1,0}^\nu)(y) h_{1,1}^{I,\nu}(y) dy - \mu_2 \boldsymbol{\nu}(1, x) \right].$$

*Remark 4.* It is easy to verify that the optimal solution of the time-discretized version of the proposed model is consistent with that of the time-continuous one. This is however not the case for the diffeomorphic motion model in [32]. As an example, at  $\tau_j = 1$ , the optimal velocity field of the time-discretized problem in [32] satisfies

$$\boldsymbol{\nu}(1, x) = \frac{1}{\mu_2} \int_{\Omega} \mathbf{K}(x, y) \nabla (I \circ \phi_{1,0}^\nu)(y) h_{1,1}^{I,\nu}(y) dy.$$

However, as derived in section 3.3.2, the optimal velocity field at  $t = 1$  of its time-continuous problem satisfies  $\boldsymbol{\nu}(1, x) = 0$ . This obviously causes inconsistencies and our consistent approach is an advantage compared to the approach in [32].

Finally, algorithm 2 outlines the procedure for computing the gradient descent scheme (62) that makes use of the above derivations.

---

**Algorithm 2** Gradient descent scheme for minimizing  $\mathcal{E}_I(\boldsymbol{\nu})$  in (47)

---

- 1: *Initialize:*
- 2:  $k \leftarrow 0$ .
- 3:  $t_i \leftarrow \frac{i}{N}$  for  $i = 0, 1, \dots, N$ .
- 4:  $\tau_j \leftarrow \frac{j}{MN}$  for  $j = 0, 1, \dots, MN$ .
- 5: Fixed  $I$ .
- 6:  $\boldsymbol{\nu}^k(\tau_i) \leftarrow \boldsymbol{\nu}^0(\tau_i)$ , where  $\boldsymbol{\nu}^0$  is a given initial velocity field.
- 7: Fixed kernel function  $K(\cdot, \cdot)$ .
- 8: Shape regularization parameter  $\mu_2 > 0$ .
- 9: Error tolerance  $\epsilon_{\boldsymbol{\nu}} > 0$ , stepsize  $\beta^k = \beta > 0$ , and maximum iterations  $K_{\boldsymbol{\nu}} > 0$ .
- 10: *Loop:*
- 11: Update  $I \circ \phi_{\tau_j, 0}^{\boldsymbol{\nu}^k}$  for  $1 \leq j \leq MN$  by

$$I \circ \phi_{\tau_j, 0}^{\boldsymbol{\nu}^k} \leftarrow (I \circ \phi_{\tau_{j-1}, 0}^{\boldsymbol{\nu}^k}) \circ \left( \text{Id} - \frac{1}{N} \boldsymbol{\nu}^k(\tau_j, \cdot) \right)$$

with  $I \circ \phi_{0, 0}^{\boldsymbol{\nu}^k} = I$ .

- 12: Update  $h_{t_i, t_i}^{I, \boldsymbol{\nu}^k}$  for  $1 \leq i \leq N$  by

$$h_{t_i, t_i}^{I, \boldsymbol{\nu}^k} \leftarrow \mathcal{T}_{t_i}^* (\mathcal{T}_{t_i} (I \circ \phi_{t_i, 0}^{\boldsymbol{\nu}^k}) - g(t_i, \cdot)).$$

- 13: Compute  $h_{\tau_j, t_i}^{I, \boldsymbol{\nu}^k}$  for  $1 \leq i \leq N$  by

$$h_{\tau_j, t_i}^{I, \boldsymbol{\nu}^k} \leftarrow \left( 1 + \frac{1}{MN} \text{div} \boldsymbol{\nu}(\tau_j, \cdot) \right) h_{\tau_{j+1}, t_i}^{I, \boldsymbol{\nu}^k} \circ \left( \text{Id} + \frac{1}{MN} \boldsymbol{\nu}^k(\tau_j, \cdot) \right)$$

for  $j = iM - 1, iM - 2, \dots, 0$ .

- 14: Compute  $\nabla \mathcal{E}_I(\boldsymbol{\nu}^k)(\tau_j, \cdot)$  (using FFT to compute the convolution) by

$$\begin{aligned} & \nabla \mathcal{E}_I(\boldsymbol{\nu}^k)(\tau_j, x) \\ & \leftarrow -\frac{2}{N} \sum_{\{i \geq 1: t_i \geq \tau_j\}} \left[ \int_{\Omega} K(x, y) \nabla (I \circ \phi_{\tau_j, 0}^{\boldsymbol{\nu}^k})(y) h_{\tau_j, t_i}^{I, \boldsymbol{\nu}^k}(y) dy - \mu_2 \boldsymbol{\nu}^k(\tau_j, x) \right] \end{aligned}$$

for  $0 \leq j \leq MN$ .

- 15: Update  $\boldsymbol{\nu}^k(\tau_j, \cdot)$  for  $0 \leq j \leq MN$  by:

$$\boldsymbol{\nu}^{k+1}(\tau_j, \cdot) \leftarrow \boldsymbol{\nu}^k(\tau_j, \cdot) - \beta \nabla \mathcal{E}_I(\boldsymbol{\nu}^k)(\tau_j, \cdot).$$

- 16: **If**  $|\boldsymbol{\nu}^{k+1} - \boldsymbol{\nu}^k| > \epsilon_{\boldsymbol{\nu}}$  and  $k < K_{\boldsymbol{\nu}}$ , then  $k \leftarrow k + 1$ , **goto** *Loop*.
  - 17: **Output**  $\boldsymbol{\nu}^{k+1}$ .
-

#### 4.4 Alternating template reconstruction and velocity field estimation

As described in the beginning of section 4, we aim to solve (45) by an iterative scheme where iterates for  $I$  and  $\nu$  are updated in an alternating manner as in (48). Hence, at each step we solve two sub-problems, one for updating  $I$  given  $\nu$  (algorithm 1 in section 4.2) and the other for updating  $\nu$  given  $I$  (algorithm 2 in section 4.3).

The algorithms for solving the two sub-problems are iterative, so there are inner iterations for each outer iterative step that update the template and velocity field. Our ultimate aim however is to obtain the minimum of the whole model (45), even if solve each subproblem thoroughly, we may have no any benefit to arrive at the desirable solution rapidly. Hence this motives us to limit the inner iteration number to be one for solving each subproblem. The final algorithm for recovering the template and velocity field is presented in the following algorithm 3. We further analyze the computational complexity of algorithm 3.

---

**Algorithm 3** Alternately minimizing model (47)

---

- 1: *Initialize:*
  - 2: Given  $M, N$ .
  - 3:  $k \leftarrow 0$ .
  - 4:  $t_i \leftarrow \frac{i}{N}$  for  $i = 0, 1, \dots, N$ . This subdivides the time interval  $[0, 1]$  uniformly into  $N$  parts.
  - 5:  $\tau_j \leftarrow \frac{j}{MN}$  for  $j = 0, 1, \dots, MN$ . This subdivides the time interval  $[0, 1]$  uniformly into  $MN$  parts.
  - 6: Fixed kernel function  $K(\cdot, \cdot)$ .
  - 7: Given regularization parameters  $\mu_1, \mu_2 > 0$ .
  - 8:  $I^k \leftarrow I^0$ , where the template is initialized.
  - 9:  $\nu^k(\tau_i) \leftarrow 0$ , where the velocity field is initialized to a zero velocity field.
  - 10: Error tolerances  $\epsilon_I, \epsilon_\nu > 0$ , stepsizes  $\alpha^k = \alpha > 0, \beta^k = \beta > 0$ , and maximum iteration number  $K > 0$ .
  - 11: *Loop:*
  - 12: Let  $\nu = \nu^k$ . Perform Lines 10-13 in algorithm 1. Output  $I^{k+1}$ .
  - 13: Let  $I = I^{k+1}$ . Perform Lines 11-15 in algorithm 2. Output  $\nu^{k+1}$ .
  - 14: **If**  $|\nu^{k+1} - \nu^k| > \epsilon_\nu$  or  $|I^{k+1} - I^k| > \epsilon_I$ , and  $k < K$ ,
  - 15: then  $k \leftarrow k + 1$ , **goto** *Loop*.
  - 16: **Output**  $I^{k+1}, \nu^{k+1}$ .
- 

**Complexity analysis** The complexity analysis, including computational cost and space complexity, is presented for algorithm 3. Since the main part of each iteration of algorithm 3 is located on lines 12-13 (actually lines 10-13 in algorithm 1 and lines 11-15 in algorithm 2), we restrict our complexity analysis to these parts. For ease of description, suppose that  $\Omega \subset \mathbb{R}^2$  and the size of the image to be reconstructed is  $n \times n$  pixels.

On line 10 of algorithm 1 and line 11 of algorithm 2, we need to update  $I \circ \phi_{\tau_j, 0}^\nu$  for  $j = 1, \dots, MN$ . Moreover, each of them should be used to compute the gradient of the objective functional on line 14 of algorithm 2, so they need to be stored at hand. Hence, in these two steps, the computational cost is

$O(n^2MN)$  and the space complexity is  $O(n^2MN)$ .

For line 11 of algorithm 1 and line 12 of algorithm 2, the  $\eta_{t_i, t_i}^{I, \nu}$  (i.e.,  $h_{t_i, t_i}^{I, \nu}$ ) need to be updated and then stored for  $i = 1, \dots, N$ . The computational cost is  $O(n^2N_dN)$ , where  $N_d$  is the number of data points. Actually, the  $N_d$  is at least proportional to the size of  $n$ , which is often  $\sqrt{2}nN_v$  with  $N_v$  denoting the number of views. Hence, the computational cost is as much as  $O(n^3NN_v)$ . Since the calculation for the forward and backward projections is on the fly, the required space is not too demanding.

Furthermore, on line 12 of algorithm 1 and line 13 of algorithm 2, for  $i = 1, \dots, N$ , the  $\eta_{\tau_j, t_i}^{I, \nu}$  (i.e.,  $h_{\tau_j, t_i}^{I, \nu}$ ) need to be updated and stored for  $j$  from  $iM - 1$  to 0, then are used to compute the gradient of the objective functional for each time point on line 14 of algorithm 2. Therefore, the computational cost is  $O(n^2MN^2)$ . For lines 11-12 of algorithm 1 and lines 12-13 of algorithm 2, the space complexity is  $O(n^2MN^2)$ .

For line 13 of algorithm 1, we need to update  $I$  once, the computational cost is  $O(n^2N)$  and the space complexity is  $O(n^2N)$ . At each time point, the FFT is used to compute the gradient of the objective functional on line 14 of algorithm 2. Hence the computational cost for this line is  $O(MN^2n^2 \log n)$ . For line 15 of algorithm 2, we need to update a vector field at each time point. Since a vector field would take twice more memory than a scalar field on 2D domain, we spend twice more computational cost to update that. Even so, the computational cost is  $O(n^2MN)$  and the space complexity is  $O(n^2MN)$ .

In summary, for algorithm 3, the computational cost is at least  $O(n^3N)$  and the space complexity is  $O(n^2MN^2)$ .

## 5 Numerical experiments

In this section, the proposed method for joint image reconstruction and motion estimation is applied to parallel beam tomography with very sparse or highly noisy data in spatiotemporal (e.g., 2D + time) imaging. We use the intensity-preserving group action to consider the involved deformations. Although this is not a full evaluation, it nevertheless illustrates the performance of the proposed method. The numerical implementation is partially based on Operator Discretization Library (<http://github.com/odlgroup/odl>).

The forward operator  $\mathcal{T}_t: \mathcal{X} \rightarrow \mathcal{Y}$  is realized by 2D Radon transforms, namely,

$$R(f)(\omega, x) = \int_{\mathbb{R}} f(x + s\omega) ds \quad \text{for } \omega \in S^1 \text{ and } x \in \omega^\perp,$$

where  $R$  denotes Radon transform,  $S^1$  is the unit circle and  $(\omega, x)$  determines a line on  $\mathbb{R}^2$  with direction  $\omega$  through  $x$ .

Moreover, consider  $\mathcal{V}$  as the space of vector fields that is a RKHS with a reproducing kernel represented by symmetric and positive definite Gaussian function  $K: \Omega \times \Omega \rightarrow \mathbb{M}_+^{2 \times 2}$  given as

$$K(x, y) := \exp\left(-\frac{1}{2\sigma^2}\|x - y\|_2^2\right) \begin{pmatrix} 1 & 0 \\ 0 & 1 \end{pmatrix} \quad \text{for } x, y \in \mathbb{R}^2. \quad (68)$$

The  $\sigma > 0$  acts as a kernel width.

The images of all gates are supported on  $\Omega$ . For image in each gate, the noise-free data per view is measured by evaluating the 2D parallel beam scanning

geometry. Then the additive Gaussian white noise at varying levels is added onto the noise-free data, which leads to the noise data. As in [17], the noise level in data is quantified in terms of signal-to-noise ratio (SNR) defined in logarithmic decibel (dB).

## 5.1 Test suites and results

The test suites seek to assess the performance against different noise levels, and the sensitivity against various selections of regularization parameters  $\mu_1$ ,  $\mu_2$ , and kernel width  $\sigma$ . We also compare the proposed method to TV-based static reconstruction method.

### 5.1.1 Test suite 1: Overview performance

Here we consider a test for evaluating the overview performance. This test uses a multi-object phantom with five gates (i.e.,  $N = 5$ ). The used phantom is shown in the last row of fig. 2, which is taken from [17].

The image in each gate is consisting of six separately star-like objects with grey-values over  $[0, 1]$ , which is digitized using  $438 \times 438$  pixels. The images of all gates are supported on a fixed rectangular domain  $\Omega = [-16, 16] \times [-16, 16]$ . For image in each gate, the noise-free data per view is measured by the 2D parallel beam scanning geometry with even 620 bins, which is supported on the range of  $[-24, 24]$ . For gate  $i$  ( $1 \leq i \leq N$ ), the scanning views are distributed on  $[(i-1)\pi/36, \pi + (i-1)\pi/36]$  uniformly, and the view number is 12. Then three different levels of additive Gaussian white noise are added onto the noise-free data. The resulting SNR are about 4.71dB, 7.7dB, and 14.67dB, respectively. To make clear, we show the noise-free and noise projection data of the first view for each.

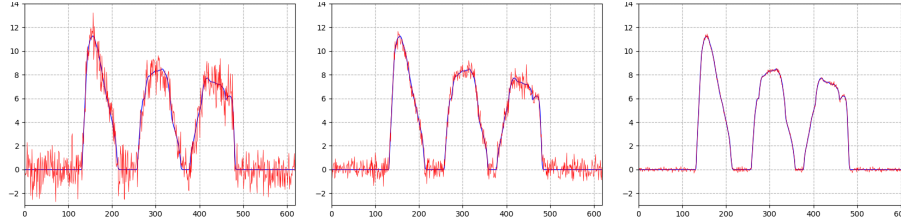


Fig. 1: Data at the first view for Gate 1. The left, middle, and right figures show data at the first view for different noise levels 4.71dB, 7.7dB, and 14.67dB, respectively. The blue smooth curve is noise-free data, and the red jagged curve is noisy data.

The factor of discretized time degree is  $M = 2$ , which is defined in section 4.2.1. The kernel width is selected to  $\sigma = 2$ . The gradient stepsizes are set as  $\alpha = 0.01$  and  $\beta = 0.05$ , respectively. First we apply algorithm 1 to obtain an initial template image after 50 iterations, then use algorithm 3 to solve the proposed model. Note that the above iteration number is not unchangeable, just needs enough to gain an appropriately initial template for algorithm 3.

The regularization parameters  $(\mu_1, \mu_2)$  are selected as  $(0.05, 10^{-7})$  for data noise level 4.71dB,  $(0.025, 10^{-7})$  for data noise level 7.7dB, and  $(0.01, 10^{-7})$  for

data noise level 14.67dB, respectively. The lower SNR, the larger value of  $\mu_1$ . The maximum iteration number is set to be 200. The reconstructed results are shown in fig. 2. It is clear that the reconstructed images (rows 1–3) are close to the corresponding ground truth, even though the data SNR is very low.

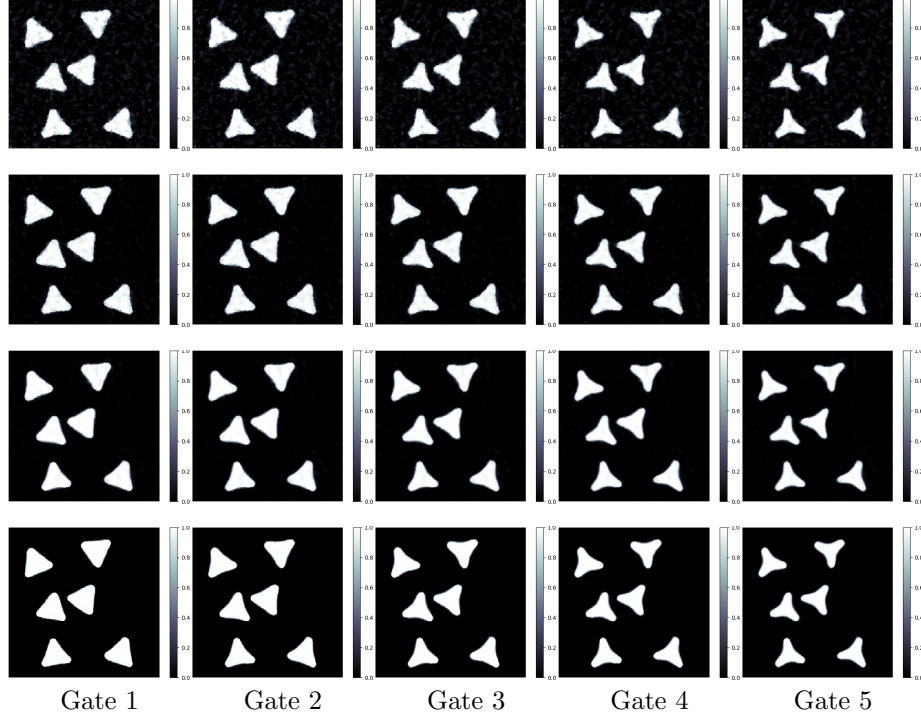


Fig. 2: Multi-object phantom. Columns represent the gates and the first three rows are reconstructed spatiotemporal images for the data with noise levels 4.71dB, 7.7dB, and 14.67dB, respectively. The last row shows the ground truth for each gate.

Apart from the visual perception, the reconstruction is quantitatively compared using structural similarity (SSIM) and peak signal-to-noise ratio (PSNR), which is frequently used to evaluate image quality [59]. The SSIM and PSNR values are tabulated in table 1. As listed in the above table, the corresponding SSIM and PSNR values are depended on SNR of the data. The higher SNR, the larger values of SSIM and PSNR.

**Comparison against static TV-regularization** It is well-known that tomographic reconstruction by TV-regularization outperforms other methods, such as filtered back projection (FBP), when the gradient of the image is sparse. This is furthermore especially notable when data is under-sampled. In our tests we use a phantom (ground truth image) that has sparse gradient, so comparing against static TV-regularization pitches our approach against one of the best static reconstruction methods.

For static TV-regularization we disregard any temporal evolution, which is equivalent to simplify the spatiotemporal problem into one with a single gate. The whole tomographic data set will then have 60 projection views. The

	Gate 1	Gate 2	Gate 3	Gate 4	Gate 5
Row 1	0.4069	0.4208	0.4273	0.4305	0.4337
	22.10	23.02	23.27	23.40	23.64
Row 2	0.5934	0.6086	0.6131	0.6149	0.6156
	25.36	27.22	27.37	27.66	27.86
Row 3	0.8411	0.8523	0.8564	0.8576	0.8587
	28.30	31.49	32.48	32.65	32.76

Tab. 1: SSIM and PSNR values of reconstructed spatiotemporal images compared to the related ground truths for the measured data with varying noise levels, see fig. 2 for detailed images. Each table entry has two values, where the upper is the value of SSIM and the bottom is the value of PSNR, which correspond to the image on the counterpart position of row 1–row3 of fig. 2.

regularization parameter for static TV-regularization is selected depending on the SNR of data in the same way as for spatiotemporal reconstruction.

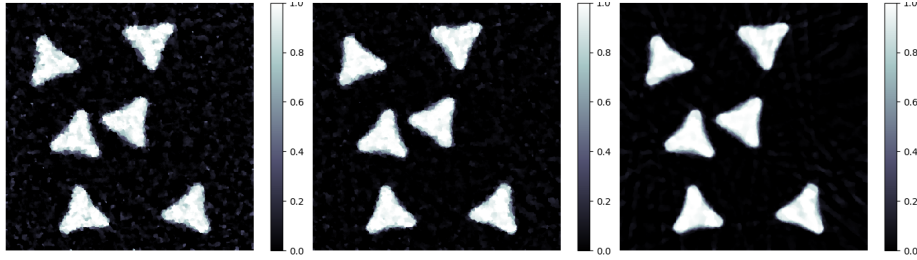


Fig. 3: TV-regularized reconstructions for the measured data with different noise levels 4.71dB (left), 7.7dB (middle), and 14.67dB (right), respectively.

Reconstructions obtained by static TV-regularization are shown in fig. 3, the edges of which are become blurring against those by our method. In addition, the corresponding SSIM and PSNR values are listed in table 2. Compared table 1 with table 2, the values of SSIM and PSNR for static TV-regularization is lower than those with the proposed method.

### 5.1.2 Test suite 2: Sensitivity against selections of regularization parameters

To solve the proposed model, three regularization parameters  $\mu_1$ ,  $\mu_2$  and  $\sigma$  need to be selected. Hence the sensitivity test should be concerned against the selections of these parameters.

As shown in the last row of fig. 4, a heart phantom with four gates (i.e.,  $N = 4$ ) is used in this test, which is originated from [30]. The image from each gate is consisting of a heart-like object with grey-values in  $[0, 1]$ , which is digitized using  $120 \times 120$  pixels. The images of all gates are supported on a fixed rectangular domain  $\Omega = [-4.5, 4.5] \times [-4.5, 4.5]$ . For image in each gate, the noise-free data per view is measured by evaluating the 2D parallel beam



	Gate 1	Gate 2	Gate 3	Gate 4	Gate 5
Left	0.3012	0.3163	0.3202	0.3146	0.3030
	18.57	19.94	20.42	19.98	18.80
Middle	0.4673	0.4867	0.4910	0.4840	0.4694
	20.44	22.82	23.76	22.90	20.79
Right	0.6004	0.6239	0.6291	0.6212	0.6029
	21.42	24.71	26.40	25.00	21.95

Tab. 2: SSIM and PSNR values of reconstructed images by TV method compared to each ground truth from Gate 1 to Gate 5 with the measured data with varying noise levels, see fig. 3 for detailed images. Each entry has two values, where the upper is the value of SSIM and the bottom is the value of PSNR.

scanning geometry with uniform 170 bins, which is supported on the range of  $[-6.4, 6.4]$ . Then the additive Gaussian white noise is added onto the noise-free data. The resulting SNR is about 14.9dB. For gate  $i$  ( $1 \leq i \leq N$ ), the scanning views are distributed on  $[(i-1)\pi/5, \pi + (i-1)\pi/5]$  evenly, which totally has 20 views. The factor of discretized time degree is  $M = 2$ . The gradient stepsizes are set as  $\alpha = 0.01$  and  $\beta = 0.05$ , respectively.

We first employ algorithm 1 to gain an initial template after 50 iterations, then use algorithm 3 to solve the proposed model. With selecting different values for regularization parameters, after 200 iterations, the reconstructed results are obtained, as shown in fig. 4. The detailed selections of varying parameter values can be referred to the caption of fig. 4. For comparison, we also present the result for static TV-regularization in fig. 5 as did in the first test. As shown in fig. 4, the related reconstructed results are almost the same and close to the counterpart ground truth. However, the reconstructed result by static TV-regularization in fig. 5 is severely degraded.

Furthermore, the SSIM and PSNR values are calculated in table 3. As given in the above table, the corresponding SSIM and PSNR values of the proposed method are relatively larger than those obtained by static TV-regularization, but are quite similar for different parameter pairs.

As shown in table 3, these values are a little bit decreased when the value of kernel parameter  $\sigma$  is changed from 1.0 to 0.5 with fixed  $\mu_1$  and  $\mu_2$ , as compared the values between row 1 and row 3, also row 2 and row 4, for instance. Therefore, this test demonstrates that to some extent the proposed method is not sensitive to the precise selection of the regularization parameters under the visual perception and the quantitative comparison (SSIM and PSNR). However, those values are selected too big or too small, which would causes over- or under-regularized results.

## 6 Conclusions and the future work

A general framework of variational model has been investigated for joint image reconstruction and motion estimation in spatiotemporal imaging, which is based on the deformable templates from shape theory. Along this framework, we proposed a new variational model for solving the above joint problem using the principle of LDDMM. The proposed model is equivalent to a PDE-constrained

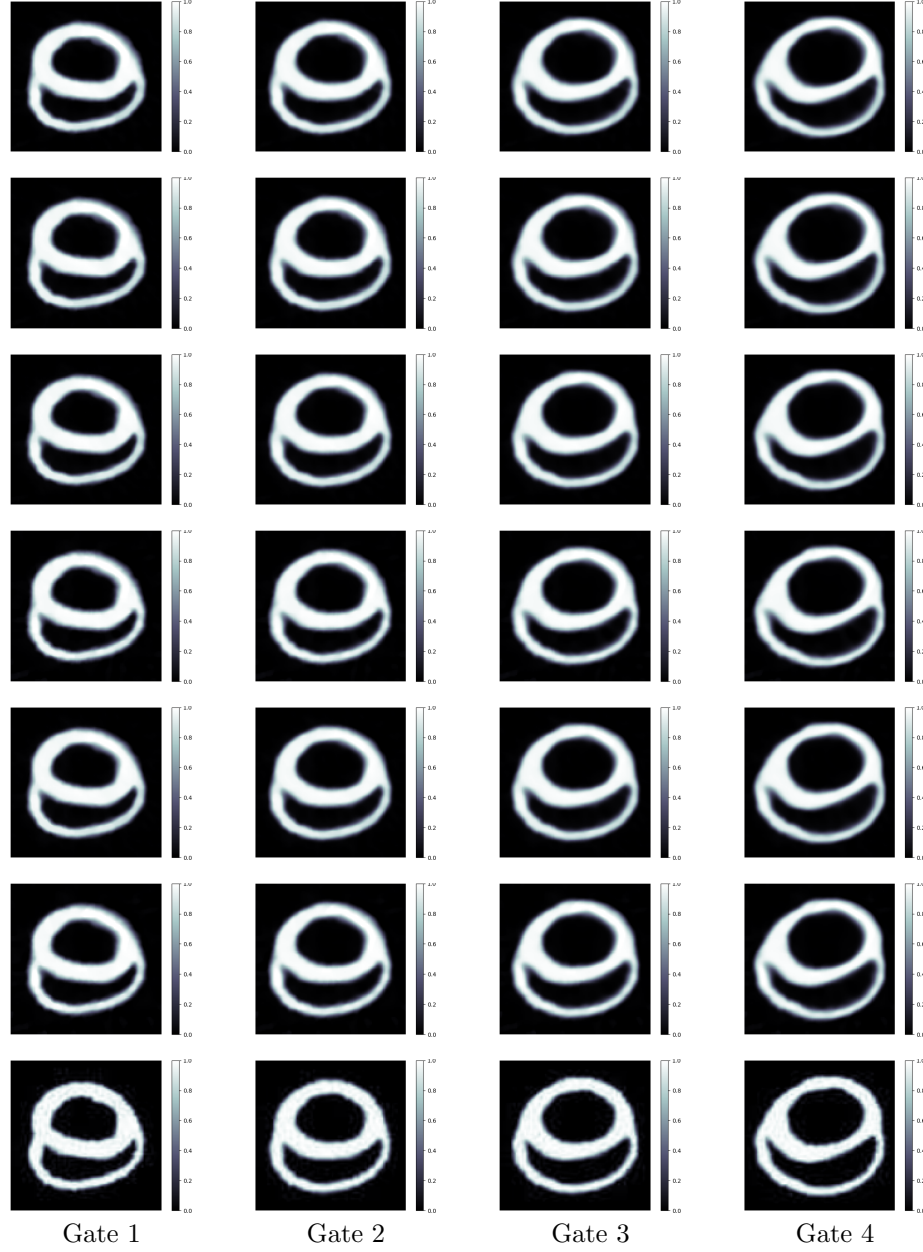


Fig. 4: Heart phantom. The columns are the 4 gates and the first 6 rows are reconstructed spatiotemporal images with parameter pairs  $(\mu_1, \mu_2, \sigma)$  chosen as  $(0.01, 10^{-7}, 1.0)$ ,  $(0.01, 10^{-6}, 1.0)$ ,  $(0.01, 10^{-7}, 0.5)$ ,  $(0.005, 10^{-7}, 0.5)$ ,  $(0.01, 10^{-6}, 0.5)$ , and  $(0.005, 10^{-6}, 0.5)$ . The last row shows the ground truth for each gate.

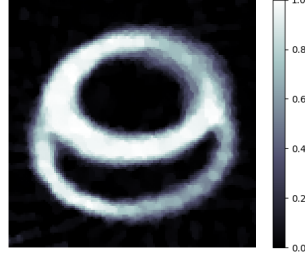


Fig. 5: Reconstruction by static TV-regulrization for the measured data with comparable noise level. The selected parameter pair  $(\mu_1, \mu_2, \sigma)$  as  $(0.005, 10^{-7}, 0.5)$ .

	Gate 1	Gate 2	Gate 3	Gate 4
Row 1	0.8928	0.9382	0.9340	0.9235
	24.25	28.44	27.64	26.28
Row 2	0.8960	0.9415	0.9346	0.9234
	24.30	28.47	27.67	26.37
Row 3	0.9103	0.9497	0.9459	0.9343
	25.33	29.41	28.97	27.78
Row 4	0.8939	0.9370	0.9357	0.9297
	25.24	29.06	28.60	27.77
Row 5	0.9087	0.9472	0.9462	0.9336
	25.14	29.30	28.83	27.68
Row 6	0.8884	0.9339	0.9358	0.9295
	25.23	29.06	28.65	27.74
TV	0.5641	0.7310	0.7458	0.5969
	14.09	19.09	18.96	14.01

Tab. 3: Row 1–row 6: SSIM and PSNR values of reconstructed spatiotemporal images compared to the related ground truths for varying values of the regularization parameters  $\mu_1$ ,  $\mu_2$ , and the kernel width  $\sigma$ , see fig. 4 for detailed images. Each entry has two values, where the upper is value of SSIM and the bottom is value of PSNR, which corresponds to the image on the counterpart position of row 1–row 6 of fig. 4. The last row: SSIM and PSNR values of reconstructed image by TV-based method compared to each ground truth from gates 1 to 4 by the measured data with comparable noise level.

optimal control problem. Based on the equivalency, we made a mathematical comparison against the joint TV-TV optical flow based model [13], which showed that our method can guarantee elastically diffeomorphic deformations, and is of benefit to the practical computation additionally. Furthermore, the theoretical comparison was also performed between the proposed model and other diffeomorphic motion models, which demonstrated that the optimal velocity field of our model is distributed w.r.t. time  $t$  averagely, and nonvanishing neither on the initial nor on the end time point. We also presented an efficiently computational method for the time-discretized version of the proposed model, which showed that its optimal solution is consistent with that of the time-continuous one, but this is not the case for the diffeomorphic motion model in [32].

An alternately gradient descent algorithm was designed to solve the time-discretized proposed model, where the main calculations were only based on the easy-implemented linearized deformations. For spatiotemporal (2D space + time) parallel beam tomographic imaging, the computational cost of the algorithm is then  $O(n^3 NN_v)$  and its memory requirement scales as  $O(n^2 MN^2)$ . With algorithm 3, we have evaluated the performance of the proposed model in dealing with the 2D space + time tomography in the case of very sparse and/or highly noisy data. As shown in these visual and quantitative results, the new method can yield reconstructed spatiotemporal images of high quality for the above difficult problems.

The future work will focus on the theoretical analysis of the proposed model, such as the existence and uniqueness of the solution, the convergence analysis of the proposed algorithm, and its extensions and applications to more complicated modalities in spatiotemporal imaging.

## A Optimality conditions

The goal is to characterize optimality conditions for (21). Let us begin with the following result.

**Lemma 1** ([60]). *Let  $\nu, \eta \in \mathcal{L}^2_{\mathcal{V}}(\Omega)$ , and  $\phi_{0,t}^\nu$  denote the solution to the ODE in (11) with given  $\nu$  at time  $t$ , and  $\phi_{s,t}^\nu$  be defined as in (14). Then,*

$$\left. \frac{d}{d\epsilon} \phi_{s,t}^{\nu+\epsilon\eta}(x) \right|_{\epsilon=0} = \int_s^t D(\phi_{\tau,t}^\nu)(\phi_{s,\tau}^\nu(x)) \left( \eta(\tau, \phi_{s,\tau}^\nu(x)) \right) d\tau \quad (69)$$

for  $x \in \Omega$  and  $0 \leq s, t \leq 1$ .

Using the result of lemma 1, we have the statement below.

**Lemma 2.** *Let the assumptions in lemma 1 hold and  $I \in \mathcal{L}^2(\Omega, \mathbb{R})$  be differentiable. Considering the group action in (4), then*

$$\left. \frac{d}{d\epsilon} (\phi_{0,t}^{\nu+\epsilon\eta}.I)(x) \right|_{\epsilon=0} = - \int_0^t \left\langle \nabla(\phi_{0,\tau}^\nu.I)(\phi_{t,\tau}^\nu(x)), \eta(\tau, \phi_{t,\tau}^\nu(x)) \right\rangle_{\mathbb{R}^n} d\tau \quad (70)$$

for  $x \in \Omega$ .

*Proof.* By chain rule we get

$$\left. \frac{d}{d\epsilon} (\phi_{0,t}^{\nu+\epsilon\eta}.I)(x) \right|_{\epsilon=0} = \left\langle \nabla I(\phi_{t,0}^\nu(x)), \left. \frac{d}{d\epsilon} \phi_{t,0}^{\nu+\epsilon\eta}(x) \right|_{\epsilon=0} \right\rangle_{\mathbb{R}^n}. \quad (71)$$

Using lemma 1, we know

$$\frac{d}{d\epsilon} \phi_{t,0}^{\nu+\epsilon\eta}(x) \Big|_{\epsilon=0} = - \int_0^t D(\phi_{\tau,0}^{\nu})(\phi_{t,\tau}^{\nu}(x)) \left( \eta(\tau, \phi_{t,\tau}^{\nu}(x)) \right) d\tau. \quad (72)$$

Inserting (72) into (71), we immediately prove (70).  $\square$

The following result is a direct consequence of the above definition and lemma 2.

**Lemma 3.** *Let the assumptions in lemma 2 hold and  $\mathcal{D}_{g_t}: \mathcal{X} \rightarrow \mathbb{R}$  be defined as (31). Assuming that  $\mathcal{D}_{g_t}$  is differentiable. Then*

$$\begin{aligned} & \frac{d}{d\epsilon} \mathcal{D}_{g_t}(\phi_{0,t}^{\nu+\epsilon\eta}.I) \Big|_{\epsilon=0} \\ &= \int_0^t \left\langle -|D(\phi_{\tau,t}^{\nu})| \nabla \mathcal{D}_{g_t}(\phi_{0,t}^{\nu}.I)(\phi_{\tau,t}^{\nu}) \nabla(\phi_{0,\tau}^{\nu}.I), \eta(\tau, \cdot) \right\rangle_{\mathcal{L}^2(\Omega, \mathbb{R}^n)} d\tau, \end{aligned} \quad (73)$$

where  $\nabla \mathcal{D}_{g_t}$  denotes the gradient of  $\mathcal{D}_{g_t}$ .

We are now ready to characterize optimality conditions for (21).

**Theorem 4.** *Let the assumptions in lemma 3 hold and  $\mathcal{E}_1: \mathcal{X} \times \mathcal{L}_{\mathcal{V}}^2(\Omega) \rightarrow \mathbb{R}$  denote the objective functional in (21), i.e.,*

$$\mathcal{E}_1(I, \nu) := \int_0^1 \left[ \mathcal{D}_{g_t}(\phi_{0,t}^{\nu}.I) + \mu_2 \int_0^t \|\nu(\tau, \cdot)\|_{\mathcal{V}}^2 d\tau \right] dt + \mu_1 \mathcal{R}_1(I). \quad (74)$$

Assuming that the regularization term  $\mathcal{R}_1$  is differentiable, and  $\mathcal{V}$  is a RKHS with a reproducing kernel  $\mathbf{K}: \Omega \times \Omega \rightarrow \mathbb{M}_+^{n \times n}$ . Then the  $\mathcal{L}_{\mathcal{V}}^2(\Omega)$ -gradient w.r.t. the velocity field  $\nu$  of  $\mathcal{E}_1(I, \cdot): \mathcal{L}_{\mathcal{V}}^2(\Omega) \rightarrow \mathbb{R}$  is

$$\begin{aligned} \nabla_{\nu} \mathcal{E}_1(I, \nu)(t, \cdot) &= \mathcal{K} \left( -\nabla(\phi_{0,t}^{\nu}.I) \int_t^1 |D(\phi_{t,\tau}^{\nu})| \nabla \mathcal{D}_{g_{\tau}}(\phi_{0,\tau}^{\nu}.I)(\phi_{t,\tau}^{\nu}) d\tau \right) \\ &\quad + 2\mu_2(1-t)\nu(t, \cdot) \end{aligned} \quad (75)$$

for  $0 \leq t \leq 1$  and where  $\mathcal{K}(\varphi) = \int_{\Omega} \mathbf{K}(\cdot, y) \varphi(y) dy$ . Furthermore, the gradient w.r.t. the template  $I$  of  $\mathcal{E}_1(\cdot, \nu): \mathcal{X} \rightarrow \mathbb{R}$  is

$$\nabla_I \mathcal{E}_1(I, \nu) = \int_0^1 |D(\phi_{0,t}^{\nu})| \nabla \mathcal{D}_{g_t}(\phi_{0,t}^{\nu}.I)(\phi_{0,t}^{\nu}) dt + \mu_1 \nabla \mathcal{R}_1(I), \quad (76)$$

where  $\nabla \mathcal{R}_1$  denotes the gradient of  $\mathcal{R}_1: \mathcal{X} \rightarrow \mathbb{R}$ . Finally, the optimality conditions for (21) read as

$$\begin{cases} \nabla_{\nu} \mathcal{E}_1(I, \nu)(t, \cdot) = 0, \\ \nabla_I \mathcal{E}_1(I, \nu) = 0. \end{cases} \quad (77)$$

*Proof.* Applying the result in lemma 3, we immediately have

$$\begin{aligned} & \frac{d}{d\epsilon} \mathcal{E}_1(I, \nu + \epsilon\eta) \Big|_{\epsilon=0} \\ &= \int_0^1 \int_0^t \left\langle -|D(\phi_{\tau,t}^{\nu})| \nabla \mathcal{D}_{g_t}(\phi_{0,t}^{\nu}.I)(\phi_{\tau,t}^{\nu}) \nabla(\phi_{0,\tau}^{\nu}.I), \eta(\tau, \cdot) \right\rangle_{\mathcal{L}^2(\Omega, \mathbb{R}^n)} d\tau dt \\ &\quad + 2\mu_2 \int_0^1 \int_0^t \langle \nu(\tau, \cdot), \eta(\tau, \cdot) \rangle_{\mathcal{V}} d\tau dt. \end{aligned}$$

Changing the order of integration in the above equation gives

$$\begin{aligned} & \frac{d}{d\epsilon} \mathcal{E}_1(I, \boldsymbol{\nu} + \epsilon \boldsymbol{\eta}) \Big|_{\epsilon=0} \\ &= \int_0^1 \left\langle -\nabla(\phi_{0,\tau}^\nu \cdot I) \int_\tau^1 |D(\phi_{\tau,t}^\nu)| \nabla \mathcal{D}_{g_t}(\phi_{0,t}^\nu \cdot I)(\phi_{\tau,t}^\nu) dt, \boldsymbol{\eta}(\tau, \cdot) \right\rangle_{\mathcal{L}^2(\Omega, \mathbb{R}^n)} d\tau \\ & \quad + 2\mu_2 \int_0^1 \langle (1-\tau)\boldsymbol{\nu}(\tau, \cdot), \boldsymbol{\eta}(\tau, \cdot) \rangle_{\mathcal{V}} d\tau. \end{aligned} \quad (78)$$

As  $\mathcal{V}$  is a RKHS with a reproducing kernel represented by  $\mathbf{K}: \Omega \times \Omega \rightarrow \mathbb{M}_+^{n \times n}$ , then

$$\langle \nu, \eta \rangle_{\mathcal{L}^2(\Omega, \mathbb{R}^n)} = \left\langle \int_\Omega \mathbf{K}(\cdot, y) \nu(y) dy, \eta \right\rangle_{\mathcal{V}} \quad \text{for } \nu, \eta \in \mathcal{V}. \quad (79)$$

Combining (78) with (79) proves (75). Finally, the results in (76) and (77) are rather straightforward to obtain, so we omit their proofs.  $\square$

## B First-order variation of $\mathcal{E}_I$

**Theorem 5.** *Let the assumptions in lemma 2 hold. Suppose  $\mathcal{E}_I: \mathcal{L}_{\mathcal{V}}^2(\Omega) \rightarrow \mathbb{R}$  is given as in (47) and  $\mathcal{V}$  is a RKHS with a reproducing kernel  $\mathbf{K}: \Omega \times \Omega \rightarrow \mathbb{M}_+^{n \times n}$ . The  $\mathcal{L}_{\mathcal{V}}^2(\Omega)$ -gradient of  $\mathcal{E}_I$  is*

$$\begin{aligned} \nabla \mathcal{E}_I(\boldsymbol{\nu})(t, x) &= -\frac{2}{N} \int_\Omega \mathbf{K}(x, y) \nabla(I \circ \phi_{t,0}^\nu)(y) \sum_{\{i \geq 1: t_i \geq t\}} h_{t,t_i}^{I,\nu}(y) dy \\ & \quad + \frac{2\mu_2}{N} \sum_{\{i \geq 1: t_i \geq t\}} \boldsymbol{\nu}_{t,t_i}(x), \end{aligned} \quad (80)$$

for  $0 \leq t \leq 1$  and  $x \in \Omega$ .

*Proof.* From lemma 2 it is not difficult to derive

$$\begin{aligned} \frac{d}{d\epsilon} \mathcal{E}_I(\boldsymbol{\nu} + \epsilon \boldsymbol{\eta}) \Big|_{\epsilon=0} &= \frac{1}{N} \sum_{i=1}^N \int_0^{t_i} \left\langle -2\eta_{\tau,t_i}^{I,\nu} \nabla(I \circ \phi_{\tau,0}^\nu), \boldsymbol{\eta}(\tau, \cdot) \right\rangle_{\mathcal{L}^2(\Omega, \mathbb{R}^n)} d\tau \\ & \quad + \frac{\mu_2}{N} \sum_{i=1}^N \int_0^{t_i} \left\langle 2\boldsymbol{\nu}(\tau, \cdot), \boldsymbol{\eta}(\tau, \cdot) \right\rangle_{\mathcal{V}} d\tau \\ &= \int_0^1 \left\langle -\frac{2}{N} \sum_{i=1}^N h_{\tau,t_i}^{I,\nu} \nabla(I \circ \phi_{\tau,0}^\nu), \boldsymbol{\eta}(\tau, \cdot) \right\rangle_{\mathcal{L}^2(\Omega, \mathbb{R}^n)} d\tau \\ & \quad + \int_0^1 \left\langle \frac{2\mu_2}{N} \sum_{i=1}^N \boldsymbol{\nu}_{\tau,t_i}(\cdot), \boldsymbol{\eta}(\tau, \cdot) \right\rangle_{\mathcal{V}} d\tau \\ &= \int_0^1 \left\langle -\frac{2}{N} \sum_{\{i \geq 1: t_i \geq t\}} h_{t,t_i}^{I,\nu} \nabla(I \circ \phi_{t,0}^\nu), \boldsymbol{\eta}(t, \cdot) \right\rangle_{\mathcal{L}^2(\Omega, \mathbb{R}^n)} dt \\ & \quad + \int_0^1 \left\langle \frac{2\mu_2}{N} \sum_{\{i \geq 1: t_i \geq t\}} \boldsymbol{\nu}_{t,t_i}(\cdot), \boldsymbol{\eta}(t, \cdot) \right\rangle_{\mathcal{V}} dt. \end{aligned}$$

The last two equations are obtained by inserting (63) and (64). Combining the above with (79) proves (80).  $\square$

## Acknowledgments

The authors would like to thank Alain Trouvé for his helpful discussions.

## References

- [1] G. Aubert and P. Kornprobst. *Mathematical Problems in Image Processing: Partial Differential Equations and the Calculus of Variations*, volume 147 of *Applied Mathematical Sciences*. Springer-Verlag, 2002.
- [2] W. Bai and M. Brady. Regularized B-spline deformable registration for respiratory motion correction in PET images. *Phys. Med. Biol.*, 54:2719–2736, 2009.
- [3] W. Bai and M. Brady. Motion correction and attenuation correction for respiratory gated PET images. *IEEE Trans. Med. Imaging*, 30(2):351–365, 2011.
- [4] H. H. Bauschke and P. L. Combettes. *Convex Analysis and Monotone Operator Theory in Hilbert Spaces*. CMS Books in Mathematics. Springer, 2ed edition, 2017.
- [5] F. M. Beg, M. I. Miller, A. Trouvé, and L. Younes. Computing large deformation metric mappings via geodesic flow of diffeomorphisms. *International Journal of Computer Vision*, 61(2):139–157, 2005.
- [6] R. Bhagalia, J. Pack, S. Miller, and M. Iatrou. Nonrigid registration-based coronary artery motion correction for cardiac computed tomography. *Med. Phys.*, 39(7):4245–4254, 2012.
- [7] M. Blume, N. Navab, and M. Rafecas. Joint image and motion reconstruction for PET using a B-spline motion model. *Phys. Med. Biol.*, 57(24):8249–8270, 2012.
- [8] M. Brehm, P. Paysan, M. Oelhafen, and M. Kachelriess. Artifact-resistant motion estimation with a patient-specific artifact model for motion-compensated cone-beam CT. *Med. Phys.*, 40(10):101913, 2013.
- [9] M. Brehm, P. Paysan, M. Oelhafen, P. Kunz, and M. Kachelriess. Self-adapting cyclic registration for motion-compensated cone-beam CT in image-guided radiation therapy. *Med. Phys.*, 39(12):7603–7618, 2012.
- [10] M. Brehm, S. Sawall, J. Maier, S. Sauppe, and M. Kachelriess. Cardiorespiratory motion-compensated micro-CT image reconstruction using an artifact model-based motion estimation. *Med. Phys.*, 42(4):1948–1958, 2015.
- [11] M. Bruveris and D. D. Holm. Geometry of image registration: The diffeomorphism group and momentum maps. In Chang D. E., D. D. Holm, G. Patrick, and T. Ratiu, editors, *Geometry, Mechanics, and Dynamics: The Legacy of Jerry Marsden*, volume 73 of *Fields Institute Communications*, pages 19–56. Springer-Verlag, 2015.
- [12] M. Bruveris and F.-X. Vialard. On completeness of groups of diffeomorphisms. *J. Eur. Math. Soc.*, 19(5):1507–1544, 2017.

- [13] M. Burger, H. Dirks, and C. Schönlieb. A Variational Model for Joint Motion Estimation and Image Reconstruction. *SIAM Journal on Imaging Sciences*, 11(1):94–128, 2018.
- [14] M. Burger, J. Modersitzki, and L. Ruthotto. A Hyperelastic Regularization Energy for Image Registration. *SIAM J. Sci. Comput.*, 35(1):B132–B148, 2013.
- [15] F. Büther, M. Dawood, L. Stegger, F. Wübbeling, M. Schäfers, O. Schober, and K. P. Schäfers. List mode-driven cardiac and respiratory gating in PET. *J. Nucl. Med.*, 50(5):674–681, 2009.
- [16] B. Chen, Z. Zhang, E. Y. Sidky, D. Xia, and X. Pan. Image reconstruction and scan configurations enabled by optimization-based algorithms in multispectral CT. *Phys. Med. Biol.*, 62:8763–8793, 2017.
- [17] C. Chen and O. Öktem. Indirect Image Registration with Large Diffeomorphic Deformations. *SIAM Journal on Imaging Sciences*, 11(1):575–617, 2018.
- [18] C. Chen and G. Xu. Gradient-flow-based semi-implicit finite-element method and its convergence analysis for image reconstruction. *Inverse Problems*, 28(3):035006, 2012.
- [19] C. Chen and G. Xu. The Linearized Split Bregman Iterative Algorithm and Its Convergence Analysis for Robust Tomographic Image Reconstruction. Technical Report 13-66, UCLA CAM Reports, 2013.
- [20] C. Chen and G. Xu. A new linearized split Bregman iterative algorithm for image reconstruction in sparse-view X-ray computed tomography. *Comput. Math. Appl.*, 71(8):1537–1559, 2016.
- [21] M. Dawood, F. Büther, X. Jiang, and K. P. Schäfers. Respiratory motion correction in 3-D PET data with advanced optical flow algorithms. *IEEE Trans. Med. Imaging*, 27(8):1164–1175, 2008.
- [22] M. Dawood, F. Büther, N. Lang, O. Schober, and K. P. Schäfers. Respiratory gating in positron emission tomography: a quantitative comparison of different gating schemes. *Med. Phys.*, 34(7):3067–3076, 2007.
- [23] M. Dawood, N. Lang, X. Jiang, and K. P. Schäfers. Lung motion correction on respiratory gated 3-d PET/CT images. *IEEE Trans. Med. Imaging*, 25:1164–1175, 2006.
- [24] M. Dawood, L. Stegger, X. Jiang, O. Schober, M. Schäfers, and K. P. Schäfers. Optimal number of respiratory gates in positron emission tomography: a cardiac patient study. *Med. Phys.*, 36(5):1775–1784, 2009.
- [25] P. Dupuis, U. Grenander, and M. Miller. Variational Problems on Flows of Diffeomorphisms for Imaging Matching. *Quarterly of Applied Mathematics*, 56(3):587–600, 1998.



- [26] W. van Elmpt, J. Hamill, J. Jones, D. De Ruyscher, P. Lambin, and M. Öllers. Optimal gating compared to 3D and 4D PET reconstruction for characterization of lung tumors. *Eur. J. Nucl. Med. Mol. Imaging*, 38:843–855, 2011.
- [27] H. Gao, J. Cai, Z. Shen, and H. Zhao. Robust principal component analysis-based four-dimensional computed tomography. *Phys. Med. Biol.*, 56:3181–3198, 2011.
- [28] F. Gigengack, X. Jiang, M. Dawood, and K. Schäfers. *Motion Correction in Thoracic Position Emission Tomography*. Springer Briefs in Electrical and Computer Engineering. Springer, 2015.
- [29] F. Gigengack, L. Ruthotto, M. Burger, C. H. Wolters, X. Jiang, and K. P. Schäfers. Motion correction in dual gated cardiac PET using mass-preserving image registration. *IEEE Trans. Med. Imaging*, 31(3):698–712, 2012.
- [30] U. Grenander and M. Miller. *Pattern Theory. From Representation to Inference*. Oxford University Press, 2007.
- [31] W. Grootjans, L.-F. de Geus-Oei, A. P. W. Meeuwis, S. Charlotte, M. Gotthardt, W. Oyen, and E. Visser. Amplitude-based optimal respiratory gating in positron emission tomography in patients with primary lung cancer. *Eur. Radio.*, 24(12):3242–3250, 2014.
- [32] J. Hinkle, M. Szegedi, B. Wang, B. Salter, and S. Joshi. 4D CT image reconstruction with diffeomorphic motion model. *Medical Image Analysis*, 16(6):1307–1316, 2012.
- [33] X. Jia, Y. Lou, B. Dong, Z. Tian, and S. Jiang. 4D computed tomography reconstruction from few-projection data via temporal non-local regularization. In T. Jiang, N. Navab, J. Pluim, and M. Viergever, editors, *Medical Image Computing and Computer-Assisted Intervention – MICCAI 2010*, volume 6361 of *Lecture Notes in Computer Science*, pages 143–150. Springer-Verlag, 2010.
- [34] N. Lang, M. Dawood, F. Büther, O. Schober, M. Schäfers, and K. P. Schäfers. Organ movement reduction in PET/CT using dual-gated list-mode acquisition. *Med. Phys.*, 16(1):93–100, 2006.
- [35] J. Liu, X. Zhang, H. Zhao, Y. Gao, D. Thomas, D. Low, and H. Gao. 5D respiratory motion model based image reconstruction algorithm for 4D cone-beam computed tomography. *Inverse Problems*, 31:115007, 2015.
- [36] G. Lucignani. Respiratory and cardiac motion correction with 4D PET imaging: shooting at moving targets. *Eur. J. Nucl. Med. Mol. Imaging*, 36(2):315–319, 2009.
- [37] M. I. Miller, A. Trounev, and L. Younes. On the metrics and Euler-Lagrange equations of computational anatomy. *Annual Reviews of Biomedical Engineering*, 4:375–405, 2002.

- [38] M. I. Miller, A. Trouné, and L. Younes. Geodesic shooting for computational anatomy. *Journal of Mathematical Imaging and Vision*, 24(2):209–228, 2006.
- [39] M. I. Miller, A. Trouné, and L. Younes. Hamiltonian systems and optimal control in computational anatomy: 100 years since D’arcy Thompson. *Annual Review of Biomedical Engineering*, 17:447–509, 2015.
- [40] F. Natterer. *The Mathematics of Computerized Tomography*, volume 32 of *Classics in Applied Mathematics*. SIAM, 2001.
- [41] H. Nien and J. A. Fessler. Fast X-ray CT image reconstruction using a linearized augmented Lagrangian method with ordered subsets. *IEEE Trans. Med. Imag.*, 34(2):388–399, 2015.
- [42] O. Öktem, C. Chen, N. O. Domaniç, P. Ravikumar, and C. Bajaj. Shape based image reconstruction using linearised deformations. *Inverse Problems*, 33(3):035004, 2017.
- [43] L. Ritschl, S. Sawall, M. Knaup, A. Hess, and M. Kachelriess. Iterative 4D cardiac micro-CT image reconstruction using an adaptive spatio-temporal sparsity prior. *Phys. Med. Biol.*, 57:1517–1525, 2012.
- [44] L. Rudin, S. Osher, and E. Fatemi. Nonlinear total variation based noise removal algorithms. *Phys. D*, 60:259–268, 1992.
- [45] O. Scherzer, M. Grasmair, H. Grossauer, M. Haltmeier, and F. Lenzen. *Variational Methods in Imaging*, volume 167 of *Applied Mathematical Sciences*. Springer-Verlag, New York, 2009.
- [46] H. Schumacher, J. Modersitzki, and B. Fischer. Combined reconstruction and motion correction in SPECT imaging. *IEEE Trans. Nucl. Sci.*, 56:73–80, 2009.
- [47] A. J. Schwarz and M. O. Leach. Implications of respiratory motion for the quantification of 2D MR spectroscopic imaging data in the abdomen. *Phys. Med. Biol.*, 45(8):2105–2116, 2000.
- [48] E. Sidky, J. Jørgensen, and X. Pan. Convex optimization problem prototyping for image reconstruction in computed tomography with the Chambolle–Pock algorithm. *Physics in medicine and biology*, 57(10):3065, 2012.
- [49] E. Sidky, C. Kao, and X. Pan. Accurate image reconstruction from few-views and limited-angle data in divergent-beam CT. *Journal of X-ray Science and Technology*, 14(2):119–139, 2006.
- [50] K. Taguchi and H. Kudo. Motion Compensated Fan-Beam Reconstruction for Nonrigid Transformation. *IEEE Trans. Med. Imaging*, 27(7):907–917, 2008.
- [51] Q. Tang, J. Cammin, S. Srivastava, and K. Taguchi. A fully four-dimensional, iterative motion estimation and compensation method for cardiac CT. *Med. Phys.*, 39(7):4291–4305, 2012.

- [52] D'Arcy Thompson. *On Growth and Form*. Cambridge University Press, New York, 1945.
- [53] A. Trouvé. Diffeomorphisms Groups and Pattern Matching in Imaging Analysis. *International Journal of Computer Vision*, 28(3):213–221, 1998.
- [54] A. Trouvé and L. Younes. Shape spaces. In S. Otmar, editor, *Handbook of Mathematical Methods in Imaging*, chapter 30, pages 1309–1362. Springer-Verlag, 2011.
- [55] A. Trouvé and L. Younes. Shape spaces. In S. Otmar, editor, *Handbook of Mathematical Methods in Imaging*, pages 1759–1817. Springer-Verlag, 2015.
- [56] A. Van Der Gucht, B. Serrano, F. Hugonnet, B. Paulmier, N. Garnier, and M. Faraggi. Impact of a new respiratory amplitude-based gating technique in evaluation of upper abdominal PET lesions. *Eur. J. Radiol.*, 83(3):509–515, 2014.
- [57] F.-X. Vialard, L. Risser, D. Rueckert, and C. J. Cotter. Diffeomorphic 3D image registration via geodesic shooting using an efficient adjoint calculation. *International Journal of Computer Vision*, 97(2):229–241, 2012.
- [58] Y. Wang, E. Vidan, and G. W. Bergman. Cardiac motion of coronary arteries: variability in the rest period and implications for coronary MR angiography. *Radiology*, 213(3):751–758, 1999.
- [59] Z. Wang, A. C. Bovik, H. R. Sheikh, and E. P. Simoncelli. Image quality assessment: From error visibility to structural similarity. *IEEE Trans. Image Process.*, 13:600–612, 2004.
- [60] L. Younes. *Shapes and Diffeomorphisms*, volume 171 of *Applied Mathematical Sciences*. Springer-Verlag, 2010.